INVESTIGATION OF NOVEL ELECTROLYTE ADDITIVES IN LITHIUM ION BATTERIES AT ELEVATED TEMPERATURE

BY

BO ZHANG

A DISSERTATION SUBMITTED IN PARTIAL FULFILLMENT OF THE REQUIREMENTS FOR THE DEGREE OF

DOCTOR OF PHILOSOPHY IN CHEMISTRY

UNIVERSITY OF RHODE ISLAND

2017

DOCTOR OF PHILOSOPHY DISSERTATION

OF

BO ZHANG

APPROVED:

Dissertation Committee:

Major Professor Brett Lucht

Louis Kirschenbaum

Arijit Bose

Nasser H. Zawia
DEAN OF THE GRADUATE SCHOOL

UNIVERSITY OF RHODE ISLAND
2017

ABSTRACT

Lithium-ion batteries (LIBs) are currently one of the leading energy storage systems behind our everyday portable devices, electric vehicles, and power grids. Due to global energy crisis and rising demands for alternative energy resources, state funded renewable energy programs and tax incentives have propelled a groundbreaking era of rapid research and development in LIBs. While we are witnessing the global shift away from conventional fossil fuels, a few major obstacles have undermined the scalability and reliability of lithium-ion batteries technology, including limited energy density, operational temperature, calendar life and safety concerns.

Among numerous attempts to circumvent the issues discussed above, developing novel electrolyte additives is one indisputably cost-effective approach in lithium-ion batteries industry. In this dissertation, we primarily focus on understanding and developing electrolyte additives to improve graphite/lithium-nickel-cobalt-manganese-oxide (NCM) cyclability and gas evolution at elevated temperature. Surface characterization techniques, such as X-ray photoelectron spectroscopy (XPS) and Fourier transform inferred spectroscopy (FTIR), are used to characterize surface chemistry of the electrodes harvested from cycled LIBs coin cells. Electrochemical impedance spectroscopy (EIS) is employed to determine the electrochemical reactivity of such additives. Further, a developed additive screening method using gas chromatography mass spectrometry (GC-MS) is implemented to study electrolyte transesterification products and monitor the changes in gas generation while incorporating novel electrolyte additives.

ACKNOWLEDGMENTS

I would like to thank my advisor, Dr. Lucht Brett for his supervision and support during my Ph.D. studies. I also want to thank my committee members, Dr. Louis Kirschenbaum, Dr. Sze Cheng Yang, Dr. Arijit Bose, and Dr. David Heskett. I am very grateful for the opportunities of working with our knowledgeable former and current group members. Thank University of Rhode Island and BASF SE for providing the research facilities and financial support.

Finally, I would like to thank my parents, my brother and my wife for their unconditional love and endless support. Because of all of you, I will always have the courage to believe - life is all about trying.

PREFACE

This dissertation is written in manuscript format. There are four chapters in this work. Chapter 1 is a brief introduction to lithium ion battery. Chapter 2 has been already published in *The Journal of Physical Chemistry C*. Both Chapter 3 and Chapter 4, written as two manuscripts respectively, will be submitted and published in the near future.

TABLE OF CONTENTS

LIST OF TABLES

TABLE PAGE

LIST OF FIGURES

CHAPTER 1

Introduction

Background

Lithium-based batteries prospered commercially in the 1960s and 1970s as a result of lithium metal ultimate electronegativity and low density [1]. The drawbacks, including lithium dendrite generation [2], internal short [3], thermal runaway andconcomitant explosion [4] have inevitably set up the threshold for a further expansion of lithium metal rechargeable technology. In the advent of replacing lithium as an anode, a novel concept of “rocking-chair” [5], also known as “shuttle-cock” [6], or “swing” batteries [7], was proposed by applying reversible chemistry to cathode materials, in which lithium ions undergoes intercalation/deintercalation without Faradaic changes (Figure 1.1). Soon carbonaceous materials were utilized as anode intercalation host [8, 9]. The energetic abundance rendered by lithium-ion intercalated carbonaceous anode and low cost of carbon have rapidly advanced the commercialization of lithium-ion batteries (LIBs). Since the milestone report on the mechanism of lithium-ion intercalation using graphitic anodes accompanied with the effect of electrolyte solvent[10], the research devoted to all essential aspects of

lithium-ion technology has enjoyed skyrocketing growth, including but not limited to the development of new carbonaceous anodes [11], transitional metal oxide cathodes [12], electrolyte systems [13, 14], and separators [15]. Despite of tremendous effort and progressive enhancement achieved in the past two decades, the current state-of-art lithium-ion batteries are far away from the perfection. Limited cycling calendar life[16], poor capacity retention during extreme temperature operations [17, 18], calamitous thermal runway and ensued explosion[19] at elevated temperature have undermined the public perspective towards lithium ion batteries and their foreseeable role in civil and military applications.

HowLIBsWork

As depicted in Figure 1.2, a conventional lithium-ion coin cell is primarily composed of cathode, anode, separator, electrolyte, current collectors, and cases.By definition, lithium-ion batteries are one family member of secondary rechargeable batteries. During the charge, an external power source is applied and a charging current flows from the positive electrode to the negative electrode within the cell. Simultaneously, the lithium ions migrate through the electrolyte and separator and intercalate into the negative electrode. During the discharge, the lithium ions travel back to the positive electrode from the negative electrode, also known as de-intercalation.

It is widely accepted that the decomposition of the electrolyte during first few charges can form a passivation layer, also known as solid electrolyte interface (SEI), and prohibit further reactions between the electrolyte and the electrodes. Despite of

numerous research efforts made in the past, the mechanism of SEI formation has not been fully understood yet. SEI is believed to be an electric insulator while facilitating ion transfer.

ElectrolyteAdditives

The development of electrolyte solvents associated with compatible salts and additives has attracted intense interest. By the very sensitive nature of electrolyte components within LIBs operating potential, carbonate-based electrolyte solvents and $LiPF_6$ have secured the de facto leading status given relatively stable electrochemical window. The very early additive approach was employed to alter surface morphology of lithium metal electrode in order to circumvent the issue associated with lithium dendrite growth[20, 21]. Considering manufacturing cost and well-established industrial supply chains, effective design and use of electrolyte additives have further become predominately active among all attempts of improving LIBs cyclability, temperature limits (-20 °C ~ 50 °C) and ion conductivity while reducing parasitic reactions [22] and hazardous risk. Since the universal adaption of the term “solid electrolyte interface” (SEI), a passive film formed on carbonaceous anodes or lithium metal anode to deter undesired electrolyte decomposition[23],numerous studies have been dedicated to resolve its mysterious formation mechanism and protective yet ion-conductive composition. Ex situ surface analysis techniques by Lucht and co-workers have suggested that the incorporation of electrolyte additives can result in quite a variety of SEI/CEI (cathode electrolyte interface) components, prevent parasitic reactions between charged electrodes and electrolyte, and reduce the dissolution of

active electrode materials into electrolyte, in combat with LIBs deterioration during elevated temperature [24, 25] and (or) high voltage operations [26, 27].

LIBs Problems and Solutions Presented in Dissertation

An emerging stake has been made by the international leaders and professionals in academia, governments and multinational corporations, to develop next generation technology of lithium-ion batteries (LIBs) amid the growing concern in global warming and the skyrocketing demand of energy storage in consumer electronics and electric vehicles (EV). Nickel-cobalt-manganese (NCM) metal oxide cathode materials have been long considered as one of the promising candidates in energy storage for EV applications. One of major shortcomings in NCM application is the discharge capacity fading and gas evolution during elevated temperature cycling.The research work presented in this dissertation starts with understanding how current state-of-art electrolyte additives (namely, 1,3-propane sultone and vinylene carbonate) improve LIBs cyclability and reduce gas generation by surface characterization techniques and on-line electrochemical mass spectrometry. Further, we have proposed a novel electrolyte additive to replace 1,3-propane sultone while forming thermally stable SEI and reducing the footprint of the carcinogenic compound. Finally, we have developed an electrolyte additive screening technique to investigate electrolyte transesterification and monitor gas evolution in high nickel NCM cells.

Reference

1. K. Xu, *Chem. Rev.*, **104**, 4303 (2004).
2. Yoshimatsu, T. Hirai and J. i. Yamaki, *J. Electrochem. Soc.*, **135**, 2422 (1988).
3. S. Tobishima and J. Yamaki, *J. Power Sources*, **81–82**, 882 (1999).
4. D. Aurbach, E. Zinigrad, H. Teller and P. Dan, *J. Electrochem. Soc.*, **147**, 1274 (2000).
5. M. Armand, in *Materials for advanced batteries*, p. 145, Springer (1980).
6. T. Ohzuku, A. Ueda and M. Nagayama, *J. Electrochem. Soc.*, **140**, 1862 (1993).
7. R. Bittihn, R. Herr and D. Hoge, *J. Power Sources*, **43**, 223 (1993).
8. T. Nagaura, M. Nagamine, I. Tanabe and N. Miyamoto, *Prog Batteries Sol Cells*, **8**, 84 (1989).
9. T. Nagaura and K. Tozawa, *Prog. Batteries Solar Cells*, **9**, 209 (1990).
10. R. Fong, U. Von Sacken and J. R. Dahn, *J. Electrochem. Soc.*, **137**, 2009 (1990).
11. Y. P. Wu, E. Rahm and R. Holze, *J. Power Sources*, **114**, 228 (2003).
12. G. A. Nazri and G. Pistoia, *Lithium batteries: science and technology*, Springer Science & Business Media (2008).
13. J. Y. Song, Y. Y. Wang and C. C. Wan, *J. Power Sources*, **77**, 183 (1999).
14. W. Li and J. R. Dahn, *J. Electrochem. Soc.*, **142**, 1742 (1995).
15. G. Venugopal, J. Moore, J. Howard and S. Pendalwar, *J. Power Sources*, **77**, 34 (1999).

16. J. Vetter, P. Novák, M. R. Wagner, C. Veit, K. C. Möller, J. O. Besenhard, M. Winter, M. Wohlfahrt-Mehrens, C. Vogler and A. Hammouche, *J. Power Sources*, **147**, 269 (2005).
17. J. Shim, R. Kostecki, T. Richardson, X. Song and K. A. Striebel, *J. Power Sources*, **112**, 222 (2002).
18. S. S. Zhang, K. Xu and T. R. Jow, *J. Power Sources*, **115**, 137 (2003).
19. Q. Wang, P. Ping, X. Zhao, G. Chu, J. Sun and C. Chen, *J. Power Sources*, **208**, 210 (2012).
20. R. D. Rauh and S. B. Brummer, *Electrochim. Acta*, **22**, 75 (1977).
21. R. Mogi, M. Inaba, S.-K. Jeong, Y. Iriyama, T. Abe and Z. Ogumi, *J. Electrochem. Soc.*, **149**, A1578 (2002).
22. Y. Matsumura, S. Wang and J. Mondori, *J. Electrochem. Soc.*, **142**, 2914 (1995).
23. E. Peled, *J. Electrochem. Soc.*, **126**, 2047 (1979).
24. C. L. Campion, W. Li and B. L. Lucht, *J. Electrochem. Soc.*, **152**, A2327 (2005).
25. M. Xu, L. Zhou, L. Hao, L. Xing, W. Li and B. L. Lucht, *J. Power Sources*, **196**, 6794 (2011).
26. L. Yang, B. Ravdel and B. L. Lucht, *Electrochem. Solid-State Lett.*, **13**, A95 (2010).
27. L. Yang, T. Markmaitree and B. L. Lucht, *J. Power Sources*, **196**, 2251 (2011).

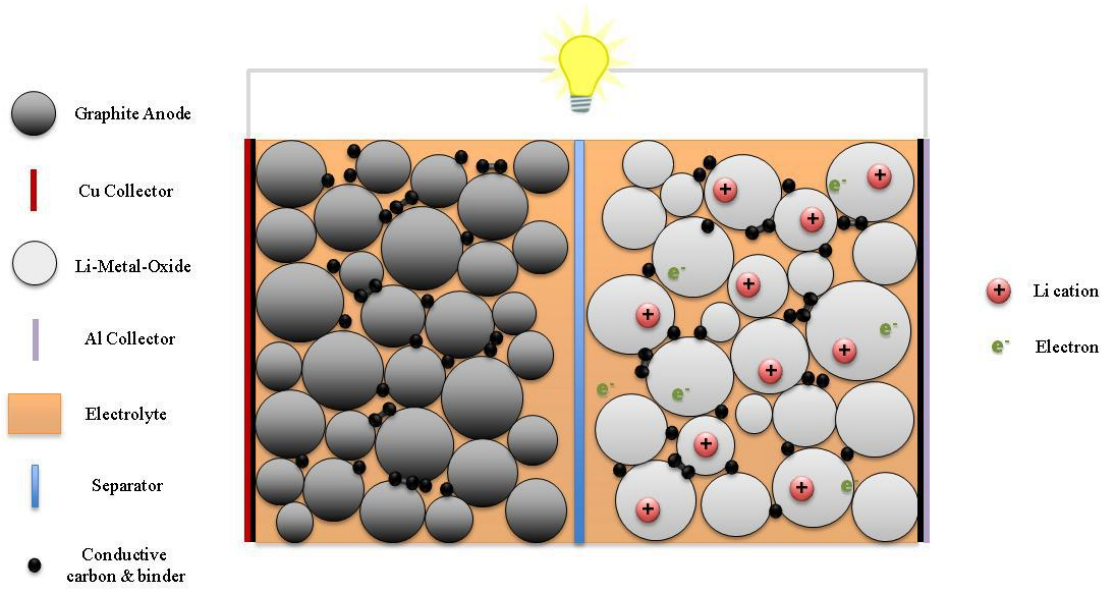

Figure 1.1 A schematic of how LIBs work

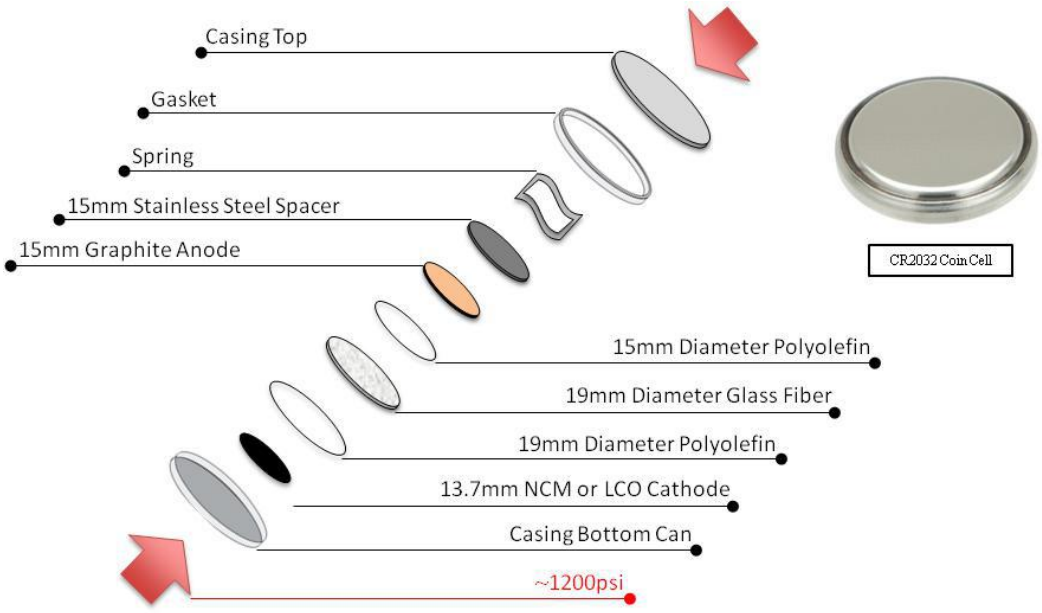

Figure 1.2 Components of a lithium-ion coin cell

CHAPTER 2

Role of 1, 3-Propane Sultone and Vinylene Carbonate in Solid Electrolyte Interface (SEI) Formation and Gas Generation

Bo Zhang[a#], Michael Metzger[d#], Sophie Solchenbach[d], Martin Payne[b], Stefano Meini[c], Hubert A. Gasteiger[d], Arnd Garsuch[c], and Brett L. Lucht[a,*]

[a]*Department of Chemistry, University of Rhode Island, Kingston, RI 02881, USA*

[b]*BASFBattery Materials,* 8001 East Pleasant Valley Rd., Independence, OH 44131

[c] *BASF SE, GCN/EE – M311, 67056 Ludwigshafen, Germany*

[d]*Chair of Technical Electrochemistry, TechnischeUniversitätMünchen, Lichtenbergstrasse 4, Garching, Germany*

[#]*the authors contributed equally to the manuscript.*

The following is published in *The Journal of Physical Chemistry C*, and presented here in manuscript format

Abstract

Lithium-ion coin cells containing electrolytes with and without 1, 3-propane sultone (PS) and vinylene carbonate (VC)have been prepared and investigated. The electrochemical performance of the cells is correlated with ex-situ surface analysis of the electrodes conducted by FTIR and XPS, and in-situ gas analysis by on-line electrochemical mass spectrometry (OEMS). The results suggest thatincorporation of both PS and VC results in improved capacity retention upon cycling at 55 °C and lower impedance.Ex-situ surface analysis and OEMSconfirm that incorporation of PS and VC alters the reduction reactions on the anode inhibiting ethylene generation and changing the structure of the solid electrolyte interface (SEI). Incorporation ofVC results in CO2 evolution, formation ofpoly(VC), and inhibition of ethylene generation. Incorporation of PS results in generation of lithium alkylsulfonate (RSO_2Li) and inhibition of ethylene generation. The combination of PS and VC reduces the ethylene gassing during formation by more than 60 %.

Introduction

Lithium-ion batteries (LIBs) are being developed forconsumer electronics, electric vehicles (EV) and other industrial energy storage devices [1], due to thehigh energy density, low self-discharge and long cycle life. However, the use of LIBs in EV applications has several critical limitations, includinglow temperature performance, calendar life performance, and safety. During the first few charge cycles of the lithium ion battery a solid electrolyte interphase (SEI) is generated on the anode surface. The SEI provides electrical insulation but lithium ion conduction. Blends of carbonates,

such as ethylene carbonate (EC) and ethyl methyl carbonate (EMC), are the preferable choice of solvents for electrolyte systems on account of thelow viscosity, high dielectric constant, good solubility of lithium salts such as $LiPF_6$, and the ability to form a stable SEI [1]. Additionally, despite the poor hydrolytic and thermal stability, $LiPF_6$remains the most widely used salt in LIBs [2].

Many investigations have been devoted to the development of novel electrolyte additives.The additives are reduced preferentially to the carbonate solvents during the first charging cycleto generate an SEI layer with superior thermal stability [3]. Vinylene carbonate (VC) is the most widely investigated electrolyte additive for EC-based electrolytes [4]. Although VC does not inhibit the thermal decomposition of $LiPF_6$ [5], the VC-derived SEI layer has been reported to have better thermal stability due to the presence of polymeric species including poly(vinylene carbonate) [6]. Unfortunately, high concentrations of VC in the electrolyte results in an increase of charge transfer resistance of the anode. The optimal VC concentration is 1~2 wt % [7]. The presence of VC has also been reported to suppress gas generationin pouch cells during formation cycling.8Incorporation of VC has also been reported to reduce gas evolution in the EC-based electrolytes and change the primary gas generated from ethylene to CO_2 [6].

Sulfur-based additives, such as sulfites and sultones have also been reported to form an SEI with better thermal stability. One of the more frequently reported sulfur containing SEI forming additives is 1,3-propane sultone (PS) [9]. PS was reported to suppress the decomposition of the propylene carbonate based electrolyte [10]. Incorporation of PS has also been reported to inhibit cell swelling after cycling at

elevated temperature [11]. However, similar to the reports of VC, incorporation of PS has been reported to increase cell resistance especially upon cycling at elevated temperature [12]. It has also been reported that the combination of VC and PS, provides better performance and reduced cell swelling than either additive independently [13]. However, an understanding of how the two different additives function cooperatively has been limited.

The cycling performance and self-discharge of graphite/$LiNi_{1/3}Co_{1/3}Mn_{1/3}O_2$ cells has been investigated for cells with and without added VC or PS and the combination of VC and PS. Ex-situ surface analysis of the electrodes was conducted via a combination of FTIR and XPS to investigate the surface chemistry on both positive and negative electrodes after formation cycling and elevated temperature cycling in orderto better understand the interrelation of PS and VC as individual additives or as a combination of additives. Furthermore, on-line electrochemical mass spectrometry (OEMS) was used to investigate gas evolution during the formation procedure. This novel combination of analytical methods has provided insight into the changes of the anode SEI upon incorporation of electrolyte additives VC and PS.

Experimental

Electrochemical measurement

Battery grade standard electrolyte (STD) 1.0 M $LiPF_6$ in EC/EMC (3/7, v/v), 1,3-propane sultone (PS), and vinylene carbonate (VC), were provided by BASFas battery grade with water content below 50 ppm.. Electrolytes with additives contain 2 wt% PS, 2 wt% VC or 2 wt% PS and 2 wt% VC added to STD. The positive electrode

$LiNi_{1/3}Co_{1/3}Mn_{1/3}O_2$ (NCM) is composed of 93% active material, 3% conductive carbon SuperP and graphite, and 4% poly(vinylidene difluoride) (PVDF)binder. The negative graphite electrode is composed of either 91% graphite(ConocoPhilips), with3% carbon super P and 6% PVDF binder or 95.7% graphitewith 0.5% carbon super P and 3.8% carboxymethyl cellulose (CMC) binder. The cycling performance of the different graphite anodes was very similar. The anodes with CMC binder were analyzed after formation cycling and the anodes with PVDF binder were analyzed after cycling at 55 °C. The electrodes were calendered.

Graphite/NCM coin cells (CR2032) were assembled using 105 µL of freshly prepared electrolyte in an argon glove-box, in which the oxygen and water contents were maintained below 0.1 ppm. Positive and negative electrode sheets were cut to a diameter of 14 mm (EL-CUT) and 14.7 mm (MTI Precision Disc Cutter T-0.6), respectively.The cathode loading is 14.6~14.8 mgNCM/cm^2. The anode loading is 15.8 mg/cm^2. And the cathode/anode area capacity ratio is 0.92~0.94. All electrodes were dried in a vacuum oven overnight at 60 °C. The positive electrode and negative electrode were centered within the coin cell can and separated withglass microfiber separator (Whatman, GE Healthcare UK Limited) with a diameter of 19 mm. Related experiments were conducted with polyolefin separators with similar results.

The graphite/$LiNi_{1/3}Co_{1/3}Mn_{1/3}O_2$ cells were cycled between 3.0 V and 4.2 V using an Arbin BT2000 battery cycler. All cells underwentinitial formation cycles including C/20 for the first cycle, C/10 for the second and third cycle, followed by 17cycles with a rate of C/5 (current density, 580 µA) at 25°C (referred to as “RT cycles”). Sequentially, another 30 elevated-temperature cycles were performed at

55°C with a cycling rate of C/5 (referred to as “ET cycles”).The potentiostatic electrochemical impedance spectra were acquired after the formation cycles.

Electrochemical Impedance

The potentiostatic electrochemical impedance measurement was carried out by BioLogic VSP at 25 °C. The impedance of all coin cells was acquired at 3.0 V with excitation sinus amplitude Va= 10 mV and frequency range 20 mHz ~ 300 kHz.

Surface analysis

The cycled cells were dismantled in an argon glove-box. The harvested positive and negative electrodes were rinsed four times with anhydrous dimethyl carbonate (DMC) to remove residual electrolyte and vacuum dried overnightto remove excess DMC. X-ray photoelectron spectroscopy (XPS) analysis was carried out on a PHI 5500 system with a focused monochromatized Al Kαradiation ($h\upsilon$ = 1486.6 eV)beam under ultrahigh vacuum (8.1×10^{-8} Pa). The spectra were collected with constant pass energy of 15 eV. XPS peakswere processed by Multipak 6.1A using the hydrocarbon contamination C1s peak at 285 eVas abinding energy reference. Element concentration was calculated based on the equation: $Cx = (Ix/Sx)/(\sum Ii/Si)$, whereIx is the relative intensity of each element, and Sx is the sensitivity number of each element.The samples were transferred from the glovebox to the XPS vacuum chamber in a sealed glass jar. The samples were exposed to air for 10-15 seconds during transfer into the XPS. All of the samples analyzed are in the discharged state. Attenuated Total Reflectance Fourier Transform Infrared Spectroscopy (ATR-FTIR) was conducted on a Bruker Tensor 27 IR spectrometer with a germanium crystal (Pike

MIRacle ATR accessory) and a room temperature DLaTGS detector. A 32-scan with a spectral resolution of 4 cm^{-1}wasacquired for each electrode under nitrogen gas flow.

Gas analysis

In-situ gas analysis by on-line electrochemical mass spectrometry (OEMS) is performed for graphite/Li metal half-cells containing the standard electrolyte and electrolyte with the additives VC and PS. For this purpose,a graphite working electrode composed of 90% graphite (SLP30, Timcal; BET area of ~7.5 m^2/g) and 10% PVDF was coated on a Celgard C480 separator (graphite loading of 6.8 mg/cm^2, at a thickness of ~100 µm) and punched to a diameter of 15 mm. The battery test cells were assembled in custom cell hardware, described recently [14-15]. It consists of a 316Ti stainless steel current collector for the lithium metal counter electrode (17 mm diameter; Rockwood Lithium, 450 µm); the graphite working electrode is contacted by a stainless steel mesh (316 SS) current collector (0.22 mm diameter wire, 1.0 mm openings, Spörl KG), which is contacted and compressed by a compression spring (316 SS, Lee Springs). Between the electrodes, two Celgard C480 separators and a Li^+-ion conductive glass ceramic (Ohara glass, Japan) were placed, and 160 µl of electrolyte containing the different additives were added. The glass ceramic serves as a diffusion barrier between anode and cathode, allowinginvestigation of the effect of the respective additive on the graphite electrode without significant interference from the Li metal electrode.

After assembly and sealing in the glove-box, the cell was placed into a climate chamber held at 25 °C (KB 20, Binder). A crimped capillary leak (Vacuum Technology Inc.) connects the OEMS cell to the mass spectrometer system (Pfeiffer

Vacuum QMA 410), permitting a constant flow of ~ 1 µl/min from the cell head space (9.5 ml) to the closed cross-beam ionization source of the mass spectrometer equipped with a secondary electron multiplier (SEM). To avoid signal fluctuations due to minor pressure/temperature changes, all mass currents were normalized to the mass current of the 36Ar isotope. The cell is first held at OCV for 2 h; subsequently a cyclic voltammetry (CV) formation procedure is applied at a san rate 0.5 mV/s (Gamry Series G300 potentiostat). The potential of the graphite electrode is ramped from OCV to 0 V vs. Li/Li^+ in the reduction step and from 0 V to 1.5 V vs. Li/Li^+ in the oxidation step. The gas evolution during three of these cycles is recorded by OEMS. Conversion of the mass spectrometer currents to concentrations was done for ethylene, carbon dioxide, and hydrogen using a calibration gas (H_2, O_2, C_2H_4 and CO_2 at 2000 ppm each in Argon, Westfalen AG).

Results

Galvanostatic cycling performance

The first formation cycle voltage versus capacity and differential capacity (dQ/dV) plots for cells containing standard electrolyte and electrolyte containing additives are depicted in Figure 2.1.The voltage versus capacity plots reveal subtle differences in the shoulders between 2.5 and 3.0 V. These differences are more apparent in the differential capacity curves consistent with significant differences in electrolyte reduction behaviors for the different electrolytes. The EC reduction peak appears at 2.95 V for the graphite/$LiNi_{1/3}Co_{1/3}Mn_{1/3}O_2$ cell without additives and is consistent with previous reports [7,16]. Incorporation of VC into the electrolyte results in the

appearance of a new reduction peak 2.85 V [7, 17]. The gas analysis discussed later suggests that the 100 mV lower reduction peak cannot be attributed to the reduction of VC, but is rather the shifted reduction peak of EC. The reduction of VCon a graphite anode at lower cell potential of 2.6 V(i.e., at higher graphite potential) than that observed for EC is consistent with an SEI layer containing the reduction products of VC [4]

The cycling performance of graphite/$LiNi_{1/3}Co_{1/3}Mn_{1/3}O_2$(NCM) cells with standard electrolyte and electrolytes with additives are presented in Figure 2.2. Similar results have been reported by Xia et al [18]. The cell with standard electrolyte has a slightly better first-cycle coulombic efficiency (80.3 %) than the cells with 2 wt% VC (76.2 %), 2 wt% PS (75.1 %),or 2 wt% PS + 2 wt% VC (75.7 %).The graphite/NCM cells containing standard electrolyte and electrolytes with additives yield stable cycling at 25 °Cwith a discharge capacity around 130mAh·g^{-1}.However, significant capacity fade is observed for cells cycled at 55°C. The cells containing electrolyte with addedVC or PS + VC have less capacity fade than cells cycled with the standard electrolyte or electrolyte with added PS (Figure 2.2).

The discharge curves after cycling at 25°C (20th cycle) and 55°C (50th cycle) are depicted in Figure 2.3.The discharge curves are very similar for all cells after cycling at 25 °C. However, the discharge curves differ after cycling at 55°C. Cells containing VC or PS + VC have larger plateausbetween 4.0 and 3.5 V consistent with the improved capacity retention. Cells containing standard electrolyteor with added PS have larger polarization which could contribute to capacity loss.

Related storage experiments were conducted. Cells were charged to 4.20 V vs Li/Li^+ and stored for 7 days at 60 °C to investigate the effect of the additives on shelf life. The results are summarized in Table 1.1. Storage of the cell containing the standard electrolyte results in a decrease in both the cell voltage (4.11 V) and the discharge capacity (94.0 % retention). However, incorporation of VC or VC + PS results in a significant improvement in the cell performance.Incorporation of VC inhibits the decrease in cell voltage (4.13 V) and improves the capacity retention to 95.5 %. Incorporation of VC and PS further inhibits the decrease in cell voltage (4.14 V) and improves capacity retention to 98.4 %. Similar results were observed by Xia et al. [18] and Petibon et al. [19].

Electrochemical Impedance Spectroscopy

The electrochemical impedance spectra acquired after the formation cycles are depicted in Figure 2.4. The incorporation of VC results in a significant increase in the cell impedance while incorporation of PS results in a decrease in the cell impedance, compared to the cell containing standard electrolyte. However, incorporation of both PS and VCresults in a decrease in cell impedance.

FTIR Analysis

The FTIR spectra of anodesextracted from cells after formation cycling and cycling at 55°C are depicted in Figure 2.5and 2.6, respectively. The IR spectrum of the fresh electrode is dominated by the CMC binder with peaks at 1030, 1410, and 1550 cm^{-1}. The electrodes extracted from cellsafter the formation cycles are similar for all of the electrolytes investigated. The peaks characteristic of CMC binder are diminished while two new peaks characteristic of Li_2CO_3(1420 cm^{-1})and lithium alkyl

carbonates (1640 cm^{-1}) are observed, consistent with the generation of an SEI on the electrode surface covering the graphite [20-21]. Some of the Li_2CO_3 could results from the decomposition of the LEDC [21]. In addition, electrodes cycled with VC contain a weak peak characteristic of poly(VC) at 1780 cm^{-1} while the cells cycled with the standard electrolyte or electrolyte with added PS contain a very weak peak characteristic of poly(carbonate) at 1780 cm^{-1}[22]. Thus polycarbonates are observed in low levels on all anodes investigated, but the concentration is increased with added VC.

Significant differences are observed for the IR spectra of the electrodes cycled with different electrolytes after cycling at 55°C. Peaks characteristic of the PVDF binder are present in all spectra at 1050 and 860 cm^{-1}.The spectrum for the electrode cycled with the standard electrolyte contains decreased absorptions characteristic of lithium alkyl carbonates. Incorporation of VC or PS + VC result in an increase in the intensity of the absorption at 1780 cm^{-1} consistent with the presence of poly(VC) [6]. A relative decrease in the intensity of the peak at 1580 cm^{-1} is also observed, suggesting the incorporation of VC results in a significant structural change to the anode SEI and that the poly(VC) structure is similar with or without added PS.

The surfaces of the cathodes extracted from cells cycled with each of the different electrolytes were also investigated by FTIR. In contrast to the observations on the anode surfaces, the FTIR spectra of the cathode surfaces are very similar for all electrolytes.

XPS Analysis

The C1s, F1s, O1s, and S2pXPS spectra of the fresh anodes and anodesextracted after formation cyclingare depicted in Figure 2.7 and the atomic concentrations as summarized in Table 1.2.In the fresh C1s spectrum, the peak at 284.3 eV is assigned to graphite, and the peak at 286.7 eV is attributed to C-O in the CMC binder. The fresh O spectra contains two peaks at 533.2 eV and 531.8 eV, due to the presence of C-O and C=O in the CMC binder. Anodes extracted from cells containing the standard electrolyte contain new C1s peaks consistent with the generation of an SEI. The standard electrolyte contains new peaks at 289-290eV (C=O, CO3-) and 287 eV (C-O) consistent with the presence of lithium alkyl carbonates and Li_2CO_3, as previously reported [19]. The C1s spectra of the electrodes cycled with PS or PS and VC are similar to the electrodes cycled with the standard electrolyte, while the electrode cycled with VC has an additional shoulder at 291 eV consistent with the presence of poly(VC) and a greater intensity of the peak associated with C-O bonds at 287 eV. This suggests that the presence of PS may inhibit VC reduction. The O1s spectra for all electrodes after cycling are very similar. The O1s peak has much greater intensity and is a broad peak centered at ~532 eV characteristic of a mixture of C-O and C=O containing species. However, in agreement with the C1s data the electrode cycled with the electrolyte containing added VC has greater intensity of the O1s peak at 535eV characteristic of poly(VC). After formation cycling, all of the electrodes contain a strong F1s peak characteristic of LiF (685 eV) and a weak peak characteristic of $Li_xPF_yO_z$ (687 eV). Electrodes cycled in the presence of PS also contain a new peak in the S2p spectrum at ~168.5 eV consistent with the presence of lithium alkylsulfonate species (R-SO_3Li) [12]. The S2p spectra are similar for all

samples containing PS while samples without PS contain no peaks in the S2p spectra.The small shoulder at 167.5 eV possibly results from XPS beam damage to the sample. The P2p spectra (not shown) are very similar for all samples and consistent with the presence of low concentrations of $Li_xPF_yO_z$.

The XPS spectra of the anodes extracted after cycling at 55 °C are depicted in Figure 2.8 and the atomic concentrations are listed in Table 1.2. The fresh electrode contains peaks characteristic of PVDF at 290.4 and 285.7 eV. The graphite signal in the C1s spectrumis significantly decreased after cycling at 55°Cfor all electrolytes (Figure 2.8) suggesting deposition of a thicker surface film on the anode.The peak at 289-290 is weaker and broadened consistent with the decomposition of lithium alkyl carbonates or Li_2CO_3. In addition, cells containing VC have an additional shoulder at 291 eV consistent with the presence of poly(VC). The O1s spectra are also similar to the electrodes after formation cycling. A broad peak centered at ~532 eV is observed. However, cellscontaining added VC or PS and VC have an additional high energy shoulder at 535 eV consistent with the presence of poly(VC) [23]. After cycling at 55°C (Figure 2.8),the F1s spectra reveal an increase in the concentration of $Li_xPF_yO_z$ and a relative decrease in the intensity of the LiF peak.Although this direct comparison is difficult since the electrode analyzed after formation cycling contains CMC binder while the electrode cycled at 55 °C contains PVDF binder. The sample with both VC and PS has the lowest relative concentration LiF. The increase in $Li_xPF_yO_z$ is also supported by the increase concentration of P on the surface as indicated in Table 1.2 further supporting a thickening of the anode SEI. The S2p spectra of electrodes cycled with PS or VC and PS reveal the presence of a peak at

168.5 eV characteristic of lithium alkylsulfonate. The intensity of the peak is weaker than that observed for the electrodes after formation cycling which may be consistent with a thicker anode SEI where the lithium sulfonates are present primarily in the inner SEI.

The surfaces of the cathodes extracted from cells cycled with each of the different electrolytes were also investigated by XPS. In contrast to the observations on the anode surfaces, the XPS spectra and elemental concentrations of the cathode surfaces are very similar for all electrolytes. An increased concentration of phosphorus is observed for all electrodes cycled at 55°C, consistent with more decomposition of $LiPF_6$.A low concentration of sulfur is also detected on the electrodes extracted from all cells cycled with PS containing electrolytes.

The results of ex-situ surface analysis indicate the SEI is generated during formation cycling and becomes thicker upon cycling at 55°C, consistent with previous reports [24-26]. Poly(VC) is observed in the IR and C1s and O1sXPS spectra of the negative electrodes cycled with the electrolytes containing VC [23]. The lithium alkylsulfonate species ($R\text{-}SO_3Li$) is observed in the S2p spectra of the negative electrodes cycled with the electrolytes containing PS [12]. The generation of either poly(VC) or lithium alkylsulfonates decrease the quantity of lithium alkyl carbonates observed on the anode surface. The presence of poly(VC) and lithium alkylsulfonate in the SEI provides both stabilization and increased lithium ion conduction as discussed below.

OEMS Analysis

The first three formation cycles of the graphite electrode versus Li metal in the standard electrolyte are shown in Figure 2.9. The upper panel of the graph displays the geometric current density as a function of the applied potential, while the middle panel shows the gas concentration in the cell,and the lower panel the gas evolution rate at the respective potential. As reported in previous studies, the main gas evolved during graphite electrode formation is ethylene, often accompanied by small amounts of hydrogen (presumably from trace water contamination [27-28] and/or of carbon monoxide [6]. The onset of ethylene evolution (represented by the m/z = 26 trace in the middle panel of Figure 2.9) appears at ~ 0.8 V vs. Li/Li^+ and it ends when the direction of the potential scan is reversed at 0 V vs. Li/Li^+. The absence of ethylene evolution during the negative-going scan (middle panel of Figure 2.9) is consistent with earlier data on thin graphite electrodes [28], on the other hand, in on-line mass spectrometry measurements from the same group with comparably thick electrodes (75-100 μm for graphite loadings of 4.5-6.6 mg/cm^2), ethylene formation was observed also during the first positive-going and the second scan [27], which was probably related to slow diffusion timesin their cell construction (note that diffusional time delays are short in our configuration due to the use of a porous separator as electrode support). In our case, there is no gas evolution during the 2nd and 3rd CV cycle (Figure2.9), which suggests that the SEI formation(at least the processes related to EC reduction) is essentially completed already after the 1st charging (negative-going) cycle. Interestingly, the shoulder in the CV profile and the maximum of the ethylene evolution rate are clearly correlated, as they both appear at ~ 0.4 V vs. Li/Li^+. The absolute amount of ethylene evolved is ~ 2150 ppm.

The amount of hydrogen evolved during the first charging cycle is very small (a maximum of ~ 200 ppm), and is likely due to the reduction of trace water (from the electrolyte and the electrodes), as was observed previously [28]. In the case of CO_2, we actually observe a consumption of ~ 200 ppm of CO_2parallel with the evolution of H_2during the first negative-going potential sweep, i.e., a consumption of the residual CO_2which was introduced into the battery head space during cell assembly in the glove-box (caused by the ~ 200 ppm CO_2 concentration in the glove box).Since H_2 evolution results in the formation of OH ions [29-30], the observed consumption of CO_2 may be due to its reaction with OH^- to form HCO_3^{2-} (and eventually Li2CO3).

Upon addition of 2 % VC to the electrolyte, a > 2 fold decrease in ethylene evolution is observed, with a total amount of ~ 850 ppm as depicted in Figure 2.10, whereby the onset of ethylene evolution in electrolyte with 2 %VC initiates at a ~ 100 mV more positive potential compared to the standard electrolyte, which would be consistent with the interpretation of the differential charge capacity plot in Figure 2.1.In contrast to the standard electrolyte, however, CO_2 is evolved once the potential is reduced below ~ 2.0 V vs. Li/Li^+, which is consistent with the gas chromatography data by Ota et al. [6],who show the presence of CO_2at 1.0 V, prior to the co-existence of CO_2 and C_2H_4 at 0.6 V and below. The continuous CO_2 production along with the consumption of VC was also reported by Petibon et. al. [31].The possible CO_2 formation mechanisms will be discussed later (see Figure2.13). CO_2evolution continues at slow but constant rate throughout the 2nd and 3rd formation cycle between 0 V and 1.5 V vs. Li/Li^+ (see Figure 2.10),despite the fact that no further

formation nor consumption of C_2H_4 can be observed after the first negative-going scan, which would suggest the formation of a dense SEI layer.

The gas evolution for the electrolyte containing 2 % PS is provided in Figure 2.11. The integral ethylene evolution reaches a maximum of ~ 800 ppm at the end of the negative-going potential scan. The onset of ethylene evolution is shifted to the lower potential again, which was observed in the standard electrolyte (~ 0.8 V vs. Li/Li^+). In contrast to VC, the formation with 2 % PS shows no CO_2 evolution. This finding supports the assumption that the reduction of VC is responsible for the evolution of CO_2.As for the other two electrolyte compositions, the SEI formation with 2 % PS seems to be completed after the first cycle, since no ethylene evolution can be seen for the subsequent cycles (data not shown). However, after the end of the ethylene evolution, a slow and steady decrease of its gas phase concentration is found over the remaining formation time. This effect can also be seen for the standard electrolyte, but not for the electrolyte containing 2 % VC.

Figure 2.12 depicts the formation of the graphite electrode in an electrolyte containing both additives, i.e.,2 % VC + 2 % PS, for whicha superposition of the above-described effects is found. Compared to the addition of only one of the additives, 2 % of both additives leads to a lower amount of ethylene gassing, whereby the onset of ethylene evolution is essentially identical to the standard electrolyte and the electrolyte with 2 % PS (~ 0.8 V vs. Li/Li+). The amount of ethylene evolved during the first cycle is ~ 700 ppm. As the electrolyte formulation contains 2 % VC, a CO_2 evolution of ~ 350 ppm is detected,similar to the case of only VC in the electrolyte. As in the case with 2 % VC, the CO_2 evolution continues throughout the

2nd and 3rd cycle (data not shown), while the amount of ethylene remains almost constant.

The total concentrations of the gaseous reaction products during the first CV formation cycle at 25 °C are listed in Table 1.3. The ethylene gassing can be substantially decreased by the addition of VC and PS. The combination of both additives leads to an even more pronounced reduction of ethylene gassing. Whenever VC is incorporated in the electrolyte, considerable amounts of CO_2 are evolved during formation.

In the case of the electrolyte with 2 % VC additive, we only observe the formation of C_2H_4, CO_2, and very minor amounts of H_2. This is in contrast to the report by Ota et al. [6], who by means of gas chromatography also detected minor amounts of CO and trace amounts of C_2H_6 and CH_4. This small discrepancy might be due to the difference in electrolyte solvent, viz., EC/DMC (1/1) in their study vs. EC/EMC (3/7) in ours. We can exclude the formation of CO in our measurements, since the intensity ratios of m/z = 28 (100 %), 27 (60 %), 26 (55 %) match the expected fractionation pattern of ethylene.So far, no mass spectrometry or gas chromatography data on the gas evolution from PS have been published, but a recent theoretical study suggested several different pathways for the reductive decomposition of PS [32], whereby propylene was proposed to be the most likely gaseous reduction product.

Discussion

The presented ex-situ surface analysis and in-situOEMS analysis confirms that the primary reduction mechanism of EC-based electrolytes is the reduction of EC to generate ethylene and lithium ethylenedicarbonate (LEDC), as originally proposed by Aurbach and co-workers (Figure 2.13) [33]. The ex-situ surface analysis suggests that LEDC and LiF are the dominant electrolyte reduction products in agreement with previous reports [20], while ethylene generation is in agreement with on-line mass spectrometry data by Imhofand Novák [29]. Our results suggest that the additives VC and PS have a strong influence on the SEI structure and gas evolution during the formation of the SEI layer. Incorporation of VC or PS results in a decrease in ethylene generation and a related decrease in LEDC on the anode surface as observed by IR and XPS.

Incorporation of 2 % VC in the electrolyte results in initial CO_2evolution at < 2.0 V vs. Li/Li^+ during the first negative-going scan, which suggests that VC is being reduced at an about 1.2 V higher potential than the EC/EMC electrolyte solvents. Ota et al. report a reductive peak related to VC at ~ 1.1 V in 1 M $LiPF_6$ EC/DMC electrolyte, leading to essentially pure CO_2 gas at 1.0 V and a mixture of CO_2 and C_2H_4 at 0.6 V [6]. Since the reductive peak related to EC beginsat ~ 0.8 V vs. Li/Li^+ [4], as observed in Figure 2.9, it appears that the evolution of C_2H_4results from EC reduction rather than VC reduction. Overall, the evolution of ethylene is lowered by ~ 60 % in the presence of VC. Upon reduction of the VC, CO_2 evolution is accompanied by poly(VC) and Li_2CO_3 generation, as observed by ex-situ analysis of the anodes. The generation of poly(VC) inhibits EC reduction to generate ethylene and LEDC.

The reason why the reductive decomposition of VC leads to CO_2 formation which is not observed during EC reduction may be related to differences in the stability of the radical anions which would result from CO_2 release from the initial radical ion produced in a one-electron reduction (see Figure 2.13): in the case of EC, CO_2 release from the initial radical anion ($\bullet CH_2\text{-}CH_2\text{-}O\text{-}COO^-$) [33] would result in a less stable radical ($\bullet CH_2\text{-}CH2\text{-}O^-$) compared to the mesomerically stabilized radical anion ($\bullet CH{=}CH\text{-}O^-$, proposed by Ota et al. [6]) which would result upon CO_2 release from the initial VC reduction product ($\bullet CH{=}CH\text{-}O\text{-}COO^-$). The stabilized radical anions couldnow attack other VC molecules in a potential independent reaction. This could happen under release of CO_2(accounting for the slow and steady increase observed in Figs. 1.10 and 1.12) to form a cross-linked polymer on the electrode surface or under retaining CO_2 to form poly(VC). At the same time, while the formation of poly(VC) in the SEI produced in the presence of VC is quite well established [6],a look to the released amount of CO_2 reveals that poly(VC) formation via reaction with$\bullet CH{=}CH\text{-}O^-$ cannot be the dominant pathway. Comparing the moles of CO_2 produced during the first charge/discharge cycle (~ 350 ppm in a volume of 9.5 ml at 25°C/1bar), amounting to 0.14 µmol, with the total amount of VC in the cell (160 µl electrolyte with 2 wt% VC), equating to ~ 37 µmol, it is clear that less than 0.4 % of the VC are following a decomposition route which leads to CO_2. Thus, it is very likely that the observed formation of CO_2 is due to a minor side reaction and does not constitute the major decomposition pathway of VC. Most of the VC is likely to directly react to poly(VC) via a nucleophilic attack by the initial VC reduction product ($\bullet CH{=}CH\text{-}O\text{-}COO^-$). This is summarized in Figure 2.13.

The addition of 2 % PS to the standard electrolyte reduces the C_2H_4 evolution rate by a factor of ~ 3 (see Table 1.3) and no CO_2 evolution is detected. Incorporation of PS has been reported to generate lithium alkylsulfonate (RSOLi) as the predominant sulfur containing reduction product of PS [9,12]. Similar sulfur containing species are observed in this investigation. In addition, the concentration of LEDC is decreased on the anode surface while the concentration of Li_2CO_3 is increased, as observed by IR and XPS spectroscopy. The decrease in LEDC correlated with the observed decrease in the ethylene generation suggests that the reduction of PS inhibits the EC reduction. The onset of ethylene evolution seems to be shifted to lower potentials of ~ 0.8 V vs. Li/Li^+ by the presence of lithium alkylsulfonates on the graphite surface. A first CV peak attributed to the reduction of PS on the graphite electrode is usually reported to be around 0.7 V vs. Li/Li^+[9, 12]. Considering the special OEMS cell hardware, this literature value is reasonably close to the experimentally found onset of gas evolution. DFT calculations on the reduction of PS suggest several decomposition pathways leading to oligomeric species, with propylene as one of the possible reduction products [32]. However, no additional gasses are generated when compared to the measurement in the standard electrolyte,suggesting that the reduction products of PS are not gaseous, but are incorporated into the SEI or dissolved into the electrolyte.

The simultaneous use of both additives leads to a superposition of the above-described phenomena. The total ethylene evolution during formation can be reduced by almost 70 %, as determined by in-situ gas analysis. This is in agreement withex-situ surface analysis, which shows that the addition of PS and VC together results in a further decrease in LEDC generation, which in turn would be consistent with a

suppression of EC reduction. In addition, the ex-situ surface analysis provides evidence for both poly(VC) and RSO_3Li on the surface of the anode, while the in-situ gas analysis provides support for CO_2 evolution resulting from the reduction of VC.Two recent articles by the group of Jeff Dahn compared the influence of VC and PS on the gas evolution in NMC/graphite pouch cells using the ex-situ Archimedes method [18, 34]. Hereit could be shown that the gas evolution during the formation procedure could be substantially reduced by the use of the additives VC and PS, especially, cells containing PS in combination with VC generate smaller volumes of gas than cells containing only PS or cells without any additive.

The performance improvements of the cells cycled with both VC and PS can be traced back to the change in the electrolyte reduction products and a resulting change in the anode SEI structure. The predominant solvent reduction products of the standard electrolyte are LEDC, Li_2CO_3, and ethylene.However, the LEDC and Li_2CO_3 are not stable upon long term cycling, especially at elevated temperature, and continuous SEI growth leads to decreasing capacity and increasing cell resistance [26]. Incorporation of VC and PS suppresses EC reduction which inhibits LEDC formation andgenerates an SEI containing both poly(VC) and lithium alkylsulfonate (RSO_3Li). The presence of the poly(VC) enhances the thermal stability of the anode SEI, while the presence of the RSO_3Li increases the ionic conductivity of the SEI. Thus the combination of the two additives creates an anode SEI with superior properties, namely,a stable cross-linked polymer with ion-conducting channels.

The eventual decrease in the ethylene signal for the standard electrolyte (Figure 2.9) and the electrolyte containing PS is not observed for the electrolyte formulations

with VC (Figure 2.10). We believe that this continuous decrease of m/z = 26 is related to the EMC component in the electrolyte, since EMC has a background signals at m/z = 26 [35]; under this assumption, one would conclude that the superior SEI formed in presence of VC is able to prevent a decomposition of EMC at the graphite electrode, leading to the observed constant m/z = 26 signal after the initial reduction cycle (Figure 2.10). Further studies to test this hypothesis are currently under investigation.

Conclusion

The cycling performance, ex-situ surface analysis, and in-situ gas analysis of lithium ion batteries containing the widely used electrolyte additives VC and PS have been investigated. All of the electrolytes have good cycling performance at 25°C. However, the electrolytes containing additiveshave better discharge capacity retentionand coulombic efficiency upon cycling at 55°C. Analysis of the differential capacity plots suggest that both VC and PS are reduced prior to EC and alter the structure of the anode SEI. Ex-situ surface analysis confirms structural differences of the anode SEI. Electrodes cycled in the presence of PS contain lithium alkylsulfonate (RSO_3Li)on the surface of the anodes. The presence of the lithium alkylsulfonate leads to higher lithium ion conductivity of the anode SEI. Electrodes cycled with added VC contain poly(VC) in the anode SEI. The presence of the poly(VC) leads to improved stability of the SEI. Anodes cycled with both VC and PS contain lithium alkylsulfonate and poly(VC) which leads to an SEI with both high conductivity and high thermal stability. In-situ gas analysis shows thatboth additives, VC and PS, are able to reduce the ethylene evolution during SEI formation by nearly70 %. The

formation of poly(VC) for electrodes cycled in VC is accompanied by CO_2 evolution. The presence of the lithium alkylsulfonate for PS leads to a lower onset potential of ethylene evolution. For VC, the only gaseous byproduct during reduction is CO_2, while PS shows no gaseous reduction products. The combination of both additives leads to a superposition of the described phenomena.The reduction of gas evolution during SEI formation would allow a faster and easierindustrial formation procedure for Li-ion batteries.

Reference

1. K. Xu, *Chem. Rev.*, **104**, 4303 (2004).
2. C. L. Campion, W. T. Li and B. L. Lucht, *J. Electrochem. Soc.*, **152**, A2327 (2005).
3. S. S. Zhang, *J. Power Sources*, **162**, 1379 (2006).
4. D. Aurbach, K. Gamolsky, B. Markovsky, Y. Gofer, M. Schmidt and U. Heider, *Electrochim. Acta*, **47**, 1423 (2002).
5. H. H. Lee, Y. Y. Wang, C. C. Wan, M. H. Yang, H. C. Wu and D. T. Shieh, *J. Appl. Electrochem.*, **35**, 615 (2005).
6. H. Ota, Y. Sakata, A. Inoue and S. Yamaguchi, *J. Electrochem. Soc.*, **151**, A1659 (2004).
7. J. C. Burns, R. Petibon, K. J. Nelson, N. N. Sinha, A. Kassam, B. M. Way and J. R. Dahn, *J. Electrochem. Soc.*, **160**, A1668 (2013).
8. J. Xia, C. P. Aiken, L. Ma, G. Y. Kim, J. C. Burns, L. P. Chen and J. R. Dahn, *Journal of the Electrochemical Society*, **161**, A1149 (2014).
9. X. X. Zuo, M. Q. Xu, W. S. Li, D. G. Su and J. S. Liu, *Electrochem. Solid-State Lett.*, **9**, A196 (2006).
10. T. Hamamoto, A. Hitaka, Y. Nakada and K. Abe, Electrolyte dissolved in a non-aqueous solvent and 0.1 to 4% by weight of a sultone derivative, in, U.S. Patent 6033809 A (2000).
11. Y. X. Guo, Z. G. Yin, Z. Y. Tao, X. H. Li and Z. X. Wang, *J. Power Sources*, **184**, 513 (2008).
12. M. Q. Xu, W. S. Li and B. L. Lucht, *J. Power Sources*, **193**, 804 (2009).

13. G. S. Han, B. Li, Z. Q. Ye, C. H. Cao and S. Y. Guan, *Int. J. Electrochem. Sci.*, **7**, 12963 (2012).

14. N. Tsiouvaras, S. Meini, I. Buchberger and H. A. Gasteiger, *J. Electrochem. Soc.*, **160**, A471 (2013).

15. S. Meini, S. Solchenbach, M. Piana and H. A. Gasteiger, *J. Electrochem. Soc.*, **161**, A1306 (2014).

16. J. O. Besenhard, M. Winter, J. Yang and W. Biberacher, *J. Power Sources*, **54**, 228 (1995).

17. J. Xia, N. N. Sinha, L. P. Chen and J. R. Dahn, *J. Electrochem. Soc.*, **161**, A264 (2014).

18. J. Xia, J. E. Harlow, R. Petibon, J. C. Burns, L. P. Chen and J. R. Dahn, *J. Electrochem. Soc.*, **161**, A547 (2014).

19. R. Petibon, N. N. Sinha, J. C. Burns, C. P. Aiken, H. Ye, C. M. VanElzen, G. Jain, S. Trussler and J. R. Dahn, *J. Power Sources*, **251**, 187 (2014).

20. M. Y. Nie, D. Chalasani, D. P. Abraham, Y. J. Chen, A. Bose and B. L. Lucht, *Journal of Physical Chemistry C*, **117**, 1257 (2013).

21. D. M. Seo, D. Chalasani, B. S. Parimalam, R. Kadam, M. Y. Nie and B. L. Lucht, *Ecs Electrochemistry Letters*, **3**, A91 (2014).

22. L. Yang, B. Ravdel and B. L. Lucht, *Electrochemical and Solid State Letters*, **13**, A95 (2010).

23. L. El Ouatani, R. Dedryvère, C. Siret, P. Biensan, S. Reynaud, P. Iratçabal and D. Gonbeau, *J. Electrochem. Soc.*, **156**, A103 (2009).

24. M. Q. Xu, L. Zhou, Y. N. Dong, Y. J. Chen, A. Garsuch and B. L. Lucht, *Journal of the Electrochemical Society*, **160**, A2005 (2013).
25. D. S. Lu, M. Q. Xu, L. Zhou, A. Garsuch and B. L. Lucht, *Journal of the Electrochemical Society*, **160**, A3138 (2013).
26. M. Herstedt, D. P. Abraham, J. B. Kerr and K. Edstrom, *Electrochimica Acta*, **49**, 5097 (2004).
27. M. Lanz and P. Novak, *J. Power Sources*, **102**, 277 (2001).
28. F. Joho, B. Rykart, R. Imhof, P. Novak, M. E. Spahr and A. Monnier, *J. Power Sources*, **81**, 243 (1999).
29. R. Imhof and P. Novak, *J. Electrochem. Soc.*, **145**, 1081 (1998).
30. R. Bernhard, S. Meini and H. A. Gasteiger, *J. Electrochem. Soc.*, **161**, A497 (2014).
31. R. Petibon, J. Xia, J. C. Burns and J. R. Dahn, *Journal of the Electrochemical Society*, **161**, A1618 (2014).
32. E. G. Leggesse and J. C. Jiang, *RSC Adv.*, **2**, 5439 (2012).
33. D. Aurbach, M. L. Daroux, P. W. Faguy and E. Yeager, *J. Electrochem. Soc.*, **134**, 1611 (1987).
34. J. Xia, L. Ma, C. P. Aiken, K. J. Nelson, L. P. Chen and J. R. Dahn, *J. Electrochem. Soc.*, **161**, A1634 (2014).

Table 2.1 The effect of the additives on LIBs shelf life

Electrolyte	Cell Voltage after 7d storage at 60°C (V)	Discharge Capacity after conditioning at 25°C (mAh/g)	Discharge Capacity after 7d storage at 60°C (mAh/g)	Capacity Retention during storage at 60°C (%)
Standard	4.11 V	134	126	94.0
2% VC	4.13 V	135	129	95.5
2% VC + 2% PS	4.14 V	132	130	98.4

Table 2.2 Atomic concentrations on the anode surface

Anode Atomic Concentration (%)		C_{1s}	O_{1s}	F_{1s}	P_{2p}	S_{2p}
Fresh Anode		85	15	0	0	0
Formation	Standard	31	64	5	1	0
	2% VC	40	55	4	0	0
	2% PS	49	43	5	1	2
	2% PS + 2% VC	39	58	2	0	1
55°C	Standard	34	23	35	8	0
	2% VC	33	28	33	6	0
	2% PS	36	24	33	6	1
	2% PS + 2% VC	43	26	27	4	1

Table 2.3 Total amounts of C_2H_4 and CO_2 evolved (or consumed) during first CV formation cycle at 25 °C and evolution/consumption rates.

Electrolyte	Integral C_2H_4 evolution [ppm]	C_2H_4 evolution rate [ppm/s]	Integral CO_2 evolution [ppm]	CO_2 evolution rate [ppm/s]
Standard	2150	2.5	-200	-0.2
2 % VC	850	1.0	350	0.25
2 % PS	800	0.8	-100	-0.1
2 % PS + 2 % VC	700	0.7	350	0.25

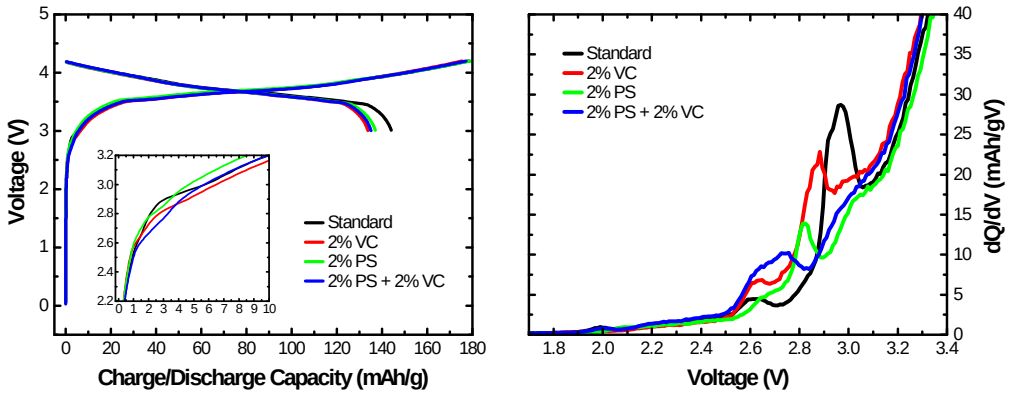

Figure 2.1 First cycle charge/discharge capacity curve and differential charge capacity curve

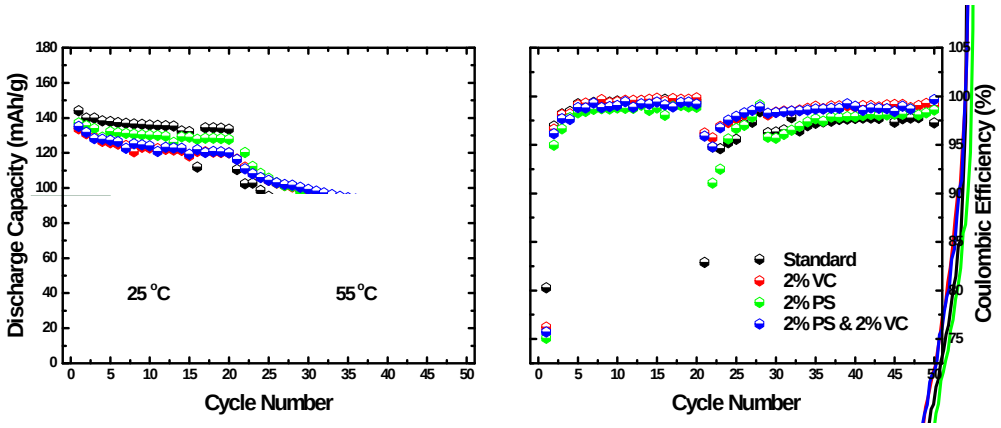

Figure 2.2 Galvanostatic cycling performance of standard electrolyte and electrolyte with additives

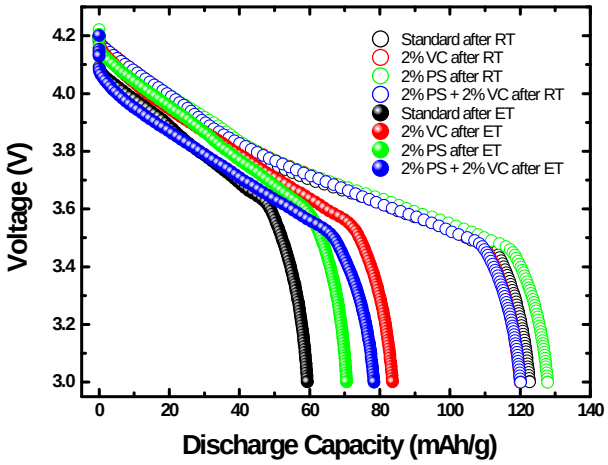

Figure 2.3 Discharge curves of the last cycle at 25 °C and 55 °C

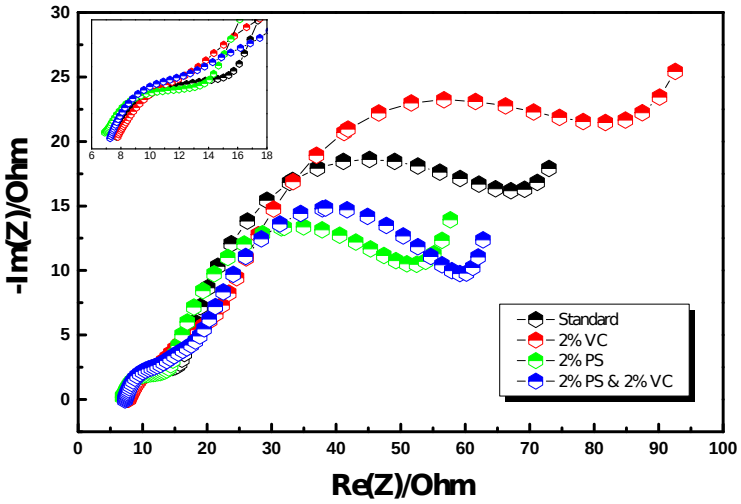

Figure 2.4 Potentiostatic electrochemical impedance measurements after the formation

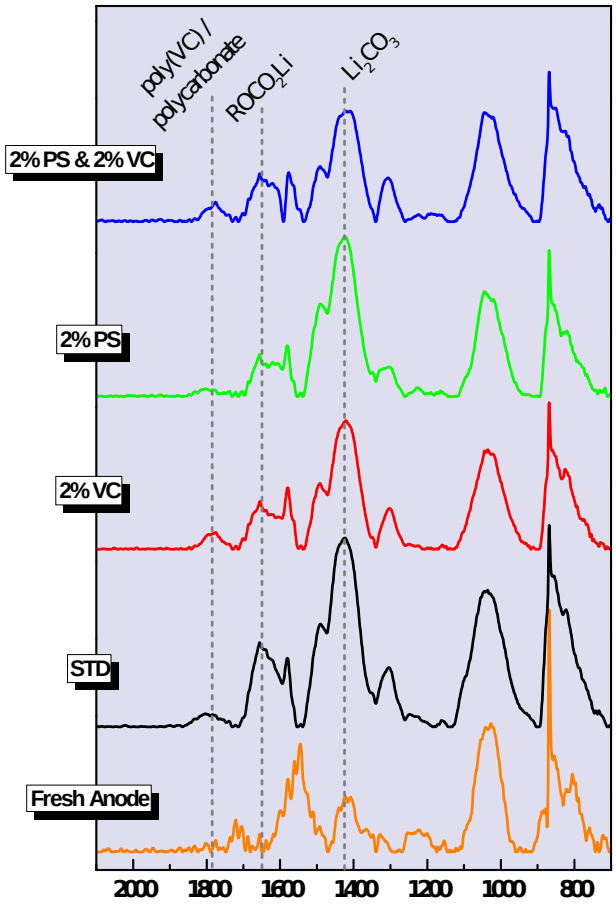

Figure 2.5 FTIR spectra of the anode surfaces after the formation

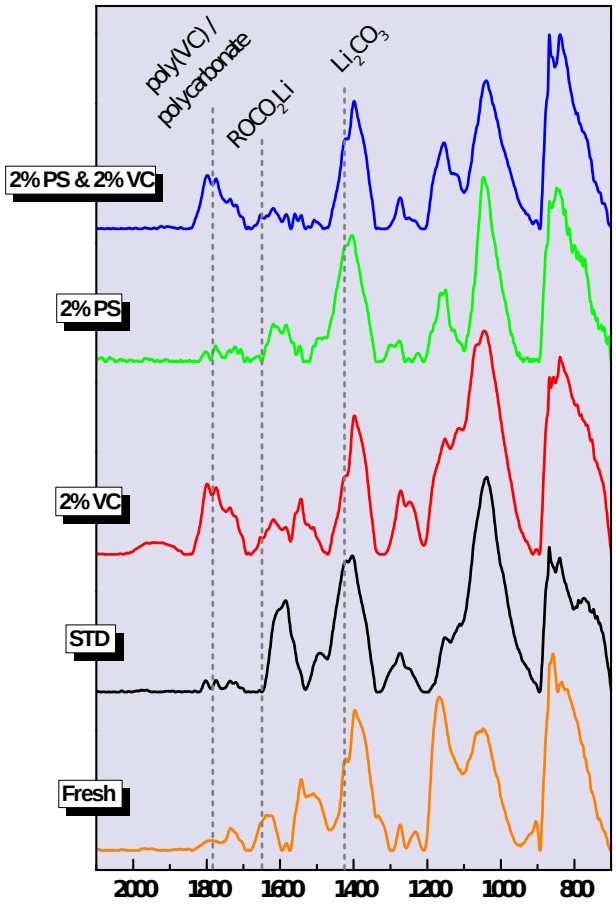

Figure 2.6 FTIR spectra of the anode surfaces after the cycling at 55°C

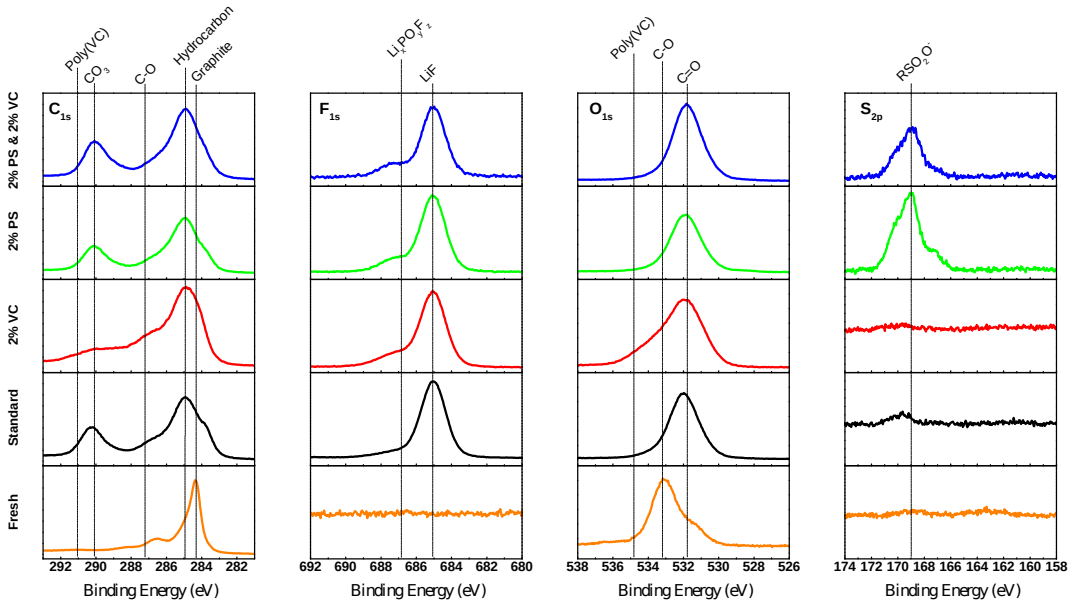

Figure 2.7 XPS analysis on the anode surface after the formation

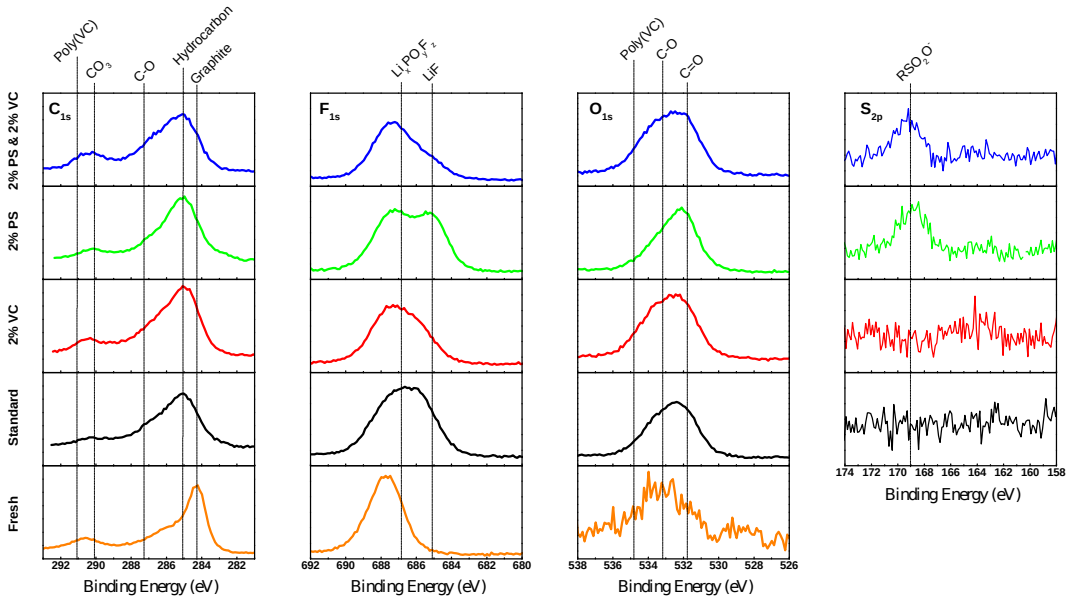

Figure 2.8 XPS analysis on the anode surface after cycling at 55°C

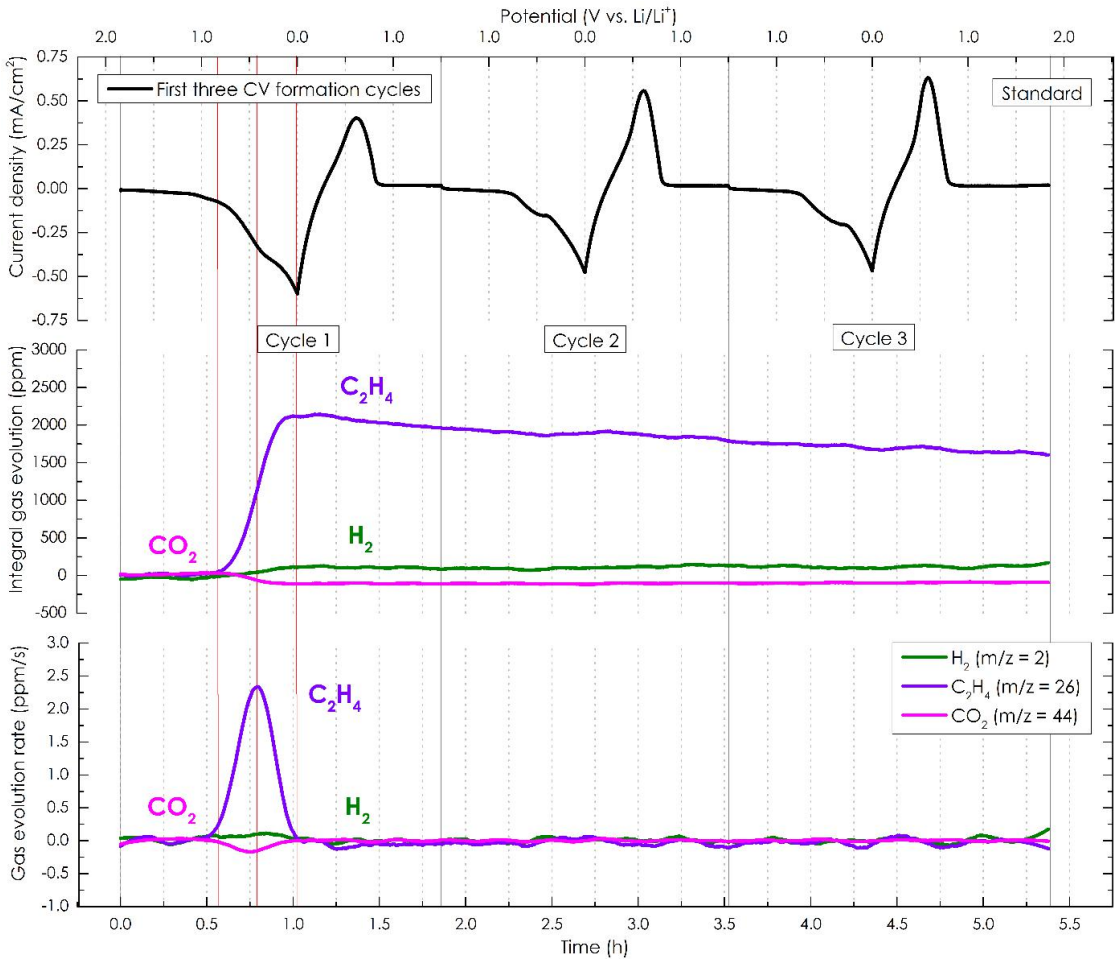

Figure 2.9 First three CV formation cycles of the graphite electrode vs. Li in 160 µl standard electrolyte at a scan rate of 0.5 mV/s at 25 °C

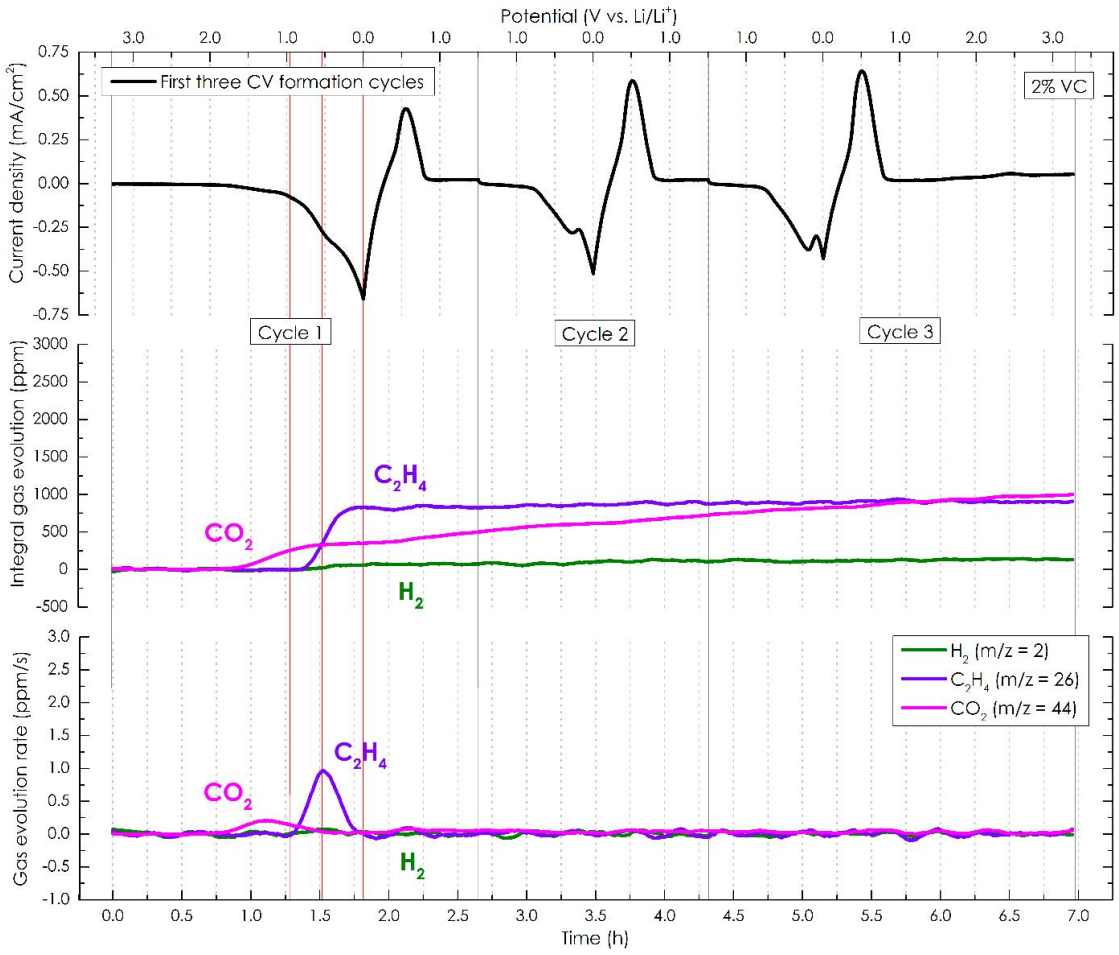

Figure 2.10 First three CV formation cycle of the graphite electrode vs. Li in 160 µl electrolyte + 2 % VC at a scan rate of 0.5 mV/s at 25 °C

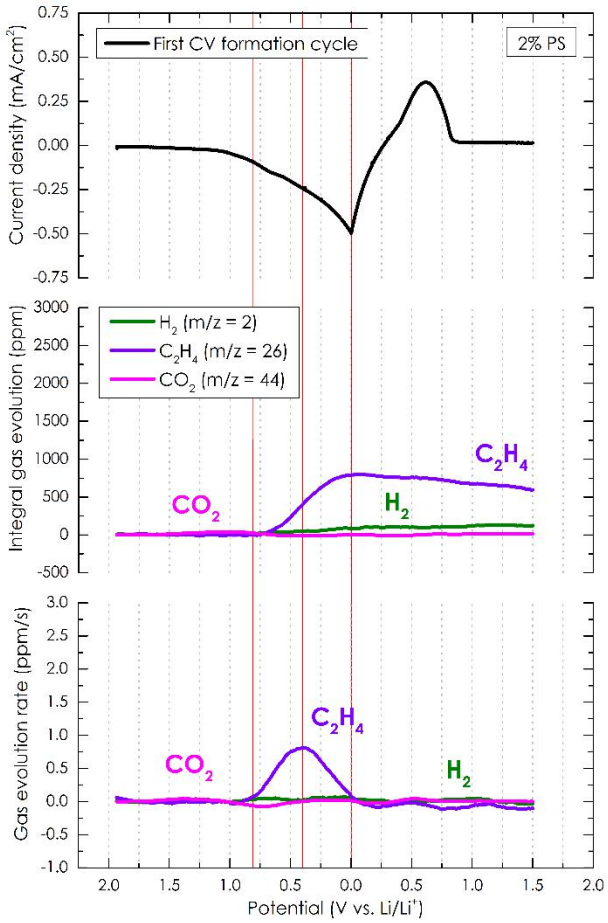

Figure2.11 First CV formation cycle of the graphite electrode vs. Li in 160 µl electrolyte + 2 % PS at a scan rate of 0.5 mV/s at 25 °C

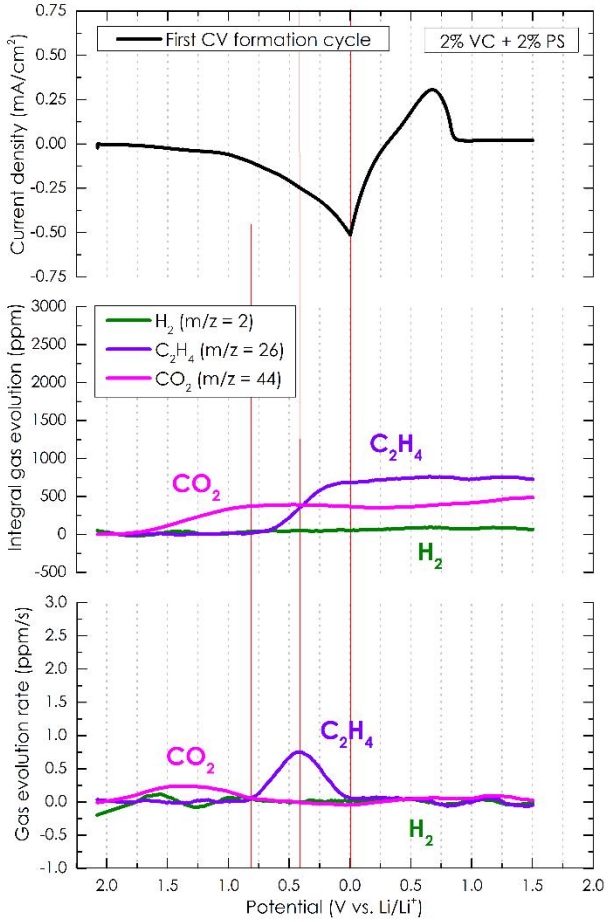

Figure 2.12 First CV formation cycle of the graphite electrode vs. Li in 160 µl electrolyte + 2 % VC + 2 % PS at a scan rate of 0.5 mV/s at 25 °C

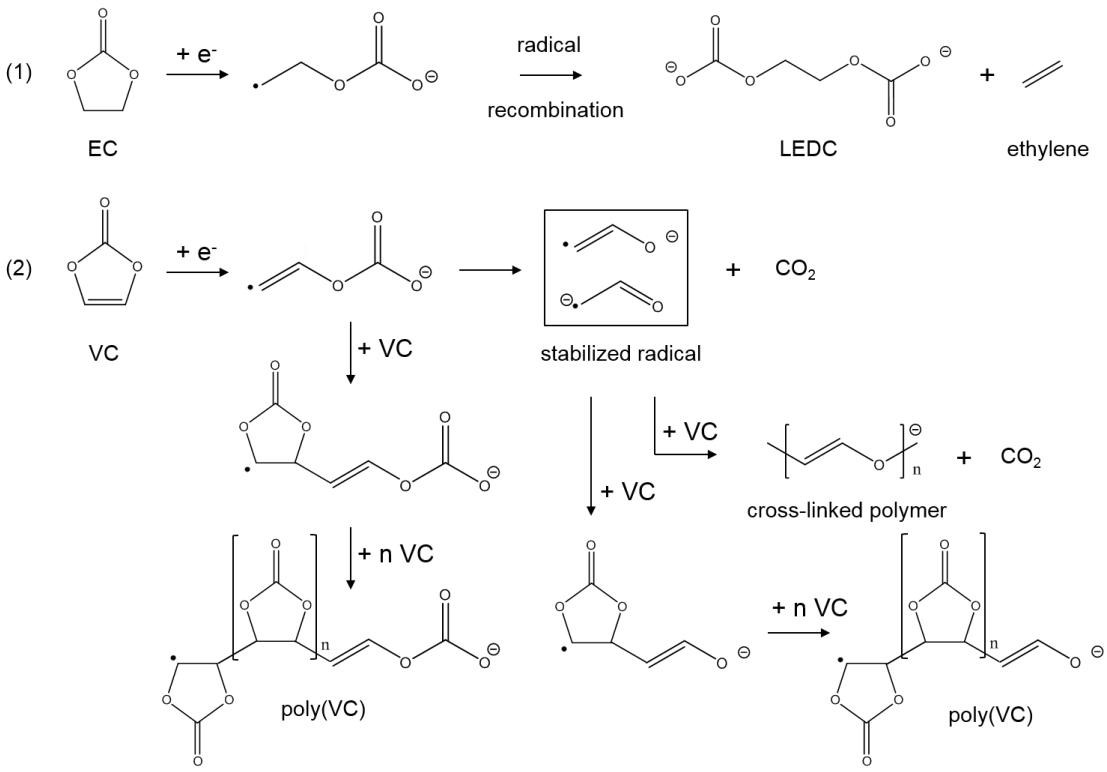

Figure 2.13 Proposed mechanism for reduction of EC (1) and VC (2)

.

CHAPTER 3

Investigation of 2, 3-Epoxypropyl Methanesulfonate (OMS) as an ElectrolyteAdditive for Lithium ion Batteries

Bo Zhang[a], Brett L. Lucht[a,*]

[a]*Department of Chemistry, University of Rhode Island, Kingston, RI 02881, USA*

The following chapter is in preparation for submission and presented here in manuscript format

Abstract

The effect of 2, 3-epoxypropyl methanesulfonate (OMS) as an electrolyte additive for lithium ion batteries (graphite/NCM) has been investigated. Lithium/graphite and lithium/NCM cells with and without added OMS were characterized by electrochemical impedance spectroscopy and differential capacity analysis.Incorporation of OMS improves discharge capacity retention by 7.5% and increases the coulombic efficiency by 2% compared to cells containing standard electrolyte for cells cycled at 55°C. The electrochemical measurements suggest that OMS reacts on the surface of the graphite anode to modify the solid electrolyte interphase (SEI). X-ray photoelectron spectroscopy (XPS)has been conducted to investigate the surface chemistry of the electrodes cycled with OMS.Surface analysis suggests that lithium alkylsulfonates, the reduction product of OMS, play a critical role in enhancing SEI thermal stability and improving capacity retention.

Introduction

Lithium ion batteries (LIB)are widely used consumer electronics due to their high energy density[1]. Significant research on lithium-ion batteries, including but not limited to the development of new carbonaceous anodes[2-6], transition metal oxide cathodes[7-9], electrolytes[10-14], lithium salts [15-19], additives[20-25], and separators[26-29], has been conducted over the last twenty years. Despite of tremendous effort and significant improvements achieved over the past two decades, the current state-of-art lithium-ion batteries still have significant limitations. Limited cycling calendar life[30], poor capacity retention during extreme temperature

operation[31, 32], and potential safety concerns[33]have limited penetration into some markets.

The development of novel electrolyte formulations composed of solvent, lithium salt, and additives has been intensely investigated for several years. The most commonly used electrolyte formulations contain $LiPF_6$ dissolved in a mixture of ethylene carbonate (EC) and dialkyl carbonates. The electrolyte components are not stable to the reduction potential of the lithiated graphite and are reduced to generate a solid electrolyte interface (SEI) which acts as a passivation layer inhibiting further electrolyte reduction but allowing lithium ion conduction[34]. The performance of the electrolyte formulations are frequently enhanced via incorporation of electrolyte additives which have been reported to improve LIBs cyclability, temperature limits (-20 ºC ~ 50 ºC) and ion conductivity while reducing parasitic reactions[35] and hazardrisk.Many electrolyte additives have been developed which are sacrificially reduced on the surface of the graphite anode to develop a superior SEI[25, 36-40].

To mitigate the co-intercalation of propylene carbonate (PC) and protect the graphite anode from exfoliation[41], incorporation of sulfur-based additivessuch as, sulfites[42-45], sulfates[46], organic sulfonates and sultones[47]have been investigated. Since theLUMO energy level of most sulfur containing additives is lower than carbonate solvents, the sulfur additives are more easily reduced. The higher reactivity of sulfur containing additives on the anode surfaceresults in preferential incorporation into the SEI. Surface analysis indicates that anodes cycled with sulfur containing additives frequently generate lithium sulfates and lithium alkyl sulfates (Li_2SO_3 and $ROSO_2Li$)[43, 48].Thus, incorporation of sulfur containing species into

the SEI has benefited LIBs in terms of longer calendar life,better capacity retention, and reduced impedance.One of the most widely used sulfur containing additives, 1,3-propane sultone(PS),is carcinogenic[49], limiting application in LIBs. However, the significant benefits ofPS in lithium ion battery electrolyteshave been widely reported [50]. We have recently developed a thorough understanding of the role of PS reduction products in the anode SEI, which has led to the development of a novel additive, 2, 3-epoxypropyl methanesulfonate(OMS, Figure 3.1), via Additives for Designed Surface Modification [51], as a potential PS replacement. An investigation of electrolyte containing OMS has been conducted in graphite/Li($Ni_{0.33}Co_{0.33}Mn_{0.33}$)$O_2$ and lithium/graphitecells. In order to better understand the role of OMS in SEI structure and function ex-situ surface analysis of the electrodes has been conducted.

Experimental

Electrochemical Measurement

The electrodes, including graphite anode and Li($Ni_{0.33}Co_{0.33}Mn_{0.33}$)$O_2$ (NCM)were prepared by a commercial supplier. The coin cell parts (i.e. cases, springs, gaskets, cans and separators) were purchased from a variety of industrial suppliers.Thebaseline electrolyte 1.2M lithium hexafluorophosphate($LiPF_6$)in EC/EMC (3:7, v/v) and 2, 3-epoxypropyl methanesulfonate (OMS) were provided by BASF as battery grade with water content below 50ppm. The positive electrode NCM is composed of 93% active material, 3% conductive carbon Super P, and 4% poly(vinylidenedifluoride) (PVDF) binder. The negative graphite electrode is composed of 95.7% graphite with 0.5% carbon super Pand 3.8% carboxymethyl

cellulose (CMC) binder. Positive and negative electrode sheets were cut into a diameter of 13.7mm (EL-CUT) and 15mm (MTI Precision Disc Cutter T-0.6), respectively. The cathode loading is 12.3mg/cm^2. The anode loading is 12.1mg/cm^2. The anode/cathode area capacity ratio is 1.13. All electrodes were dried in a vacuum oven for 24 hours at 110°C.

The general cell assembly protocols are presented as follows (unless otherwise indicated in the context, respectively). Prior to the cycling, all graphite/NCM coin cells (CR2032) were assembled with 105 µL of freshly prepared electrolyte in a sealed glove box filled with argon. The positive electrode and negative electrode were centered within the coin cell casing and isolated with a three-layer separator using 19mm diameter polyolefin, 19 mm diameter glass microfiber(Whatman, GE Healthcare UK Limited), and 15 mm diameter polyolefin in order. A MTI hydraulic crimping machine was used to finalize the inner pressure (around 1200 psi) of the cell, assuring a sufficient internal contact. The finished coin cells were stored for 12-hour at 25°C, allowing the electrode to be thoroughly wetbefore initial cycling.The assembly of lithium/graphite half cells followed thesameprocedure.

The graphite/NCM cells were cycled between 3.0 V and 4.2 V using an Arbin BT2000 battery cycler. All cells underwent initial formation cycles including C/20 for the first cycle, C/10 for the second and third cycle, followed by 17 cycles with a rate of C/5(580µA) at 25°C. Sequentially, another 50 cycles were performed at 55°C with a rate of C/5.

Electrochemical Impedance

The potentiostatic electrochemical impedance measurements were performed usingaBioLogicVSP at 25°C (± 1°C). The impedance of all coin cells was acquired at 3.0 V with excitation sinus amplitude Va= 10mV and frequency range 20mHz ~ 300kHz.

Surface Analysis (XPS)

After cyclingthe cells were transferred back to a sealed argon glove box and dismantled via a disassembling machine (MTI MSK-110D). The harvested electrodes were rinsed 3 times with anhydrous dimethyl carbonate (DMC) to remove residual electrolyte and then dried in a vacuum chamber at 25°C to remove the excess DMC.X-ray photoelectron spectroscopy (XPS) analysis was conducted on a Thermo K-Alpha system with a focused monochromatized Al Kα radiation (hυ= 1486.6eV) beam under ultrahigh vacuum (8.1×10^{-8}Pa)[52]. The electrodes were transferred from the glove box to the XPS chamber via a customized vacuum transfer vessel fromThermoScientific.Allelectrodes are analyzedin the discharged state. The spectra were collected with constant pass energy of 50 eV. XPS peaks were processed by ThermoScientificAvantage v5.932. The hydrocarbonpeak at 285 eV was usedas a binding energy referencefor the peer peak assignment.

Results and Discussion

The galvanostatic cycling performance of the cells cycled with 2 wt. % OMS, 2 wt. % PS and standard electrolyte is demonstrated in Figure 3.2. The first cycle coulombic efficiencies of all cells are well above 90%. The efficiency of cell with OMS (90.4%) is comparable to the cell cycled with PS (90.5%) but slightly lower than

cells cycled with standard electrolyte (91.5%), indicating the presence of OMS might facilitate increased yet beneficial electrolyte decomposition in the course of SEI formation. After the first formation cycle, all cells have coulombic efficiencies above 97%. All cells have similar discharge capacity upon cycling at 25°C. The cells containing standard electrolyte experiencesignificant capacity loss during cycling at 55 °C. The capacity retention decreases from 95% to 82%. However, the cell cycled with 2 wt. % OMS has only5 % capacity loss after cycling at 55 °C. The cell with 2 wt. % PS has an 8% capacity loss. Incorporation of OMS in the electrolyte results in improved cycling performance at 55 °C compared to the standard electrolyte.

The charge/discharge voltage profiles of graphite/NCM cycled with standard electrolyte and OMS-containing electrolyte are provided in Figure 3.3 at the end of the first formation cycle, after room temperature cycling (20th cycle, 25°C), and after elevated temperature cycling (60th cycle, 55°C). Both cells have a definitive charging plateau from 3.5 to 3.8 V. Similar charge/discharge curves of the first formation cycle are observed, although the cells with OMS have more irreversible capacity loss (5.4 mAh/g), which is equivalent tothe difference in coulombic efficiency. During the elevated temperature cycling (55°C), a decrease of the plateau is observedfor the cell with the standard electrolyte, whereas the decrease is lessened for the cell cycled withelectrolyte containing OMS. The charge/discharge curves are consistent with the capacity retention and suggest that incorporation of OMS prolongs the cyclability of graphite/NCM at elevated temperature.

In order to develop a better understanding of the source of the performance enhancements for cells with added OMS, lithium/graphite and lithium/NCM cells have

been assembled and cycled and the differential capacity curves are presented in Figure 3.4. Fig.3.4a shows that the cells containing the standard electrolyte exhibittwoprimary reduction peaksat 0.65V and 0.8 V, which are assigned to the reduction of EC. The altered reduction curve serves asauxiliary evidence of OMS involvement in the SEI formation. The dQ/dV plots for the Li/NCMcellscycled with or without OMS are nearly identical(Figure 3.6b), suggesting good anodic stability of OMS up to 4.2 V. The dQ/dV plots suggest that OMS modifies the SEI on the anode and has little effect on the cathode surface and thus the differences in performance are likely related to changes in the structure of the anode SEI.

Electrochemical Impedance Spectra (EIS) are depicted in Figure 3.5.The first semicircle is attributed to high frequencies and associated with the resistance of the surface layer including SEI, whereas the second semicircle is attributed to medium range frequencies and correlated to faradaic charge transfer resistance. The Warburg impedance is the short strait line at a near 45° angle at low frequencies.Thecellcycled with OMS has a smaller second semicircle, indicating lower charge transfer resistance after 20 cycles at 25°C. However, the cell with OMS has slightly larger charge transfer resistance after 40 cycles at 55°C. Overall, the incorporation of OMS does not result in a significant change of cell impedance upon cycling.

In order to develop a better understanding of the effect of OMS on the cycling performance of graphite/NMC cells, ex-situ surface analysis of the extracted electrodes was conducted. XPS spectraacquired on anodes extracted from the cell cycled with OMS after the formation, 25°C and 55°C are provided in Figure 3.6. The C1s spectrum of the fresh anode is dominated by peaks characteristic of the CMC

binder at 286.9 eV (C-O) and graphite at 284.3 eV (C-C). After the formation cycle, the graphite peak at 284.3 eV is significantly decreased and new peaks characteristic of the anode SEI are observed at 285 eV (hydrocarbon), 286.9 eV (C-O), 289 eV (C=O) and 290 eV (CO3)consistent with the presence of lithium alkyl carbonates, lithium carbonate and related species aspreviously reported[53-57]. All cycled anodes contain a strong peak characteristic of LiFat 685 eV, and a smaller peakof$Li_xPO_yF_z$at 687.3 eV with a broad shoulder. In O1s spectra (not shown), a broad peak with much greater intensity is located at ~531.5 eV characteristic of a mixture of C-O and C=O containing species. However, The XPS C1s spectra of the electrode cycled with electrolyte containing OMS is quite different. The C1s peak for graphite is diminished and the peak characteristic of C-H at 285 eV is increased, but the peak characteristic of CO_3^{2-} is very small, suggesting that incorporation of OMS inhibits the reduction of EC. In addition, acontribution of sulfur-based species is observed in the S2p spectrum consistent with the presence of lithium alkyl sulfates as previously reported for PS[50]. The data suggests that addition of OMS alters the composition of the SEI upon formation cycling, in agreement with the electrochemical measurement discussed above.

After cycling at 25°C, the electrode cycled with the standard electrolyte does not change significantly, consistent with either no change or a slight thickening of the SEI.Interestingly, after cycling at 25 °C with the electrolyte containing added OMS, new peaks are observed in the C1s spectrum characteristic of CO_3^{2-} at 290 eVsuggesting that while EC reduction is inhibited during formation cycling the SEI thickens upon additional cycling to incorporate lithium alkyl carbonates and lithium

carbonate. Sulfur containing species are still observed suggesting either a thin layer of lithium carbonates, less than the depth of penetration of XPS (~ 5 nm), or continued reduction of OMS to generate new sulfur containing species. The F1s spectra of the electrodes extracted from the cells with or without OMS are very similar although there is a slight decrease in the intensity of the$Li_xPO_yF_z$peak at 687.3 eV for cells containing added OMS. The O1s spectrum contains broad peak centered at 531.5 eV for both electrolytes consistent with the presence of lithium alkyl carbonates and lithium carbonate.

As the cycling is continued at elevated temperature, 55°C, the C1s spectrum of the electrode cycled with the standard electrolyte changes. The peak characteristic of CO_3^{2-} diminishes significantly consistent with the decomposition of lithium alkyl carbonates and Li_2CO_3 in the SEI. However, the anode cycled with electrolyte containing OMS has less change. The peak characteristic of CO_3^{2-} is slightly decreased, but the decrease is significantly less than that observed for the electrode cycled with the standard electrolyte.The smaller change in the SEI suggests that the reduction products of OMS stabilize the SEI which is consistent with the improved cycling performance (Figure 3.2). The F1s spectra are similar for both electrolytes. The O1s spectra are also similar for the electrodes cycled with both electrolytes consistent with the C1s XPS data.The S2p spectra do not change significantly consistent with the presence and stability of the reduction products of OMS,lithiumalkylsulfonates, on the anodes.

The element concentrations as determined by XPS are depicted in Table 3.1. The concentration of C onbothelectrodes extracted from cells cycled at 25 °C containing

either the standard orOMSelectrolytesare relatively constant around 21% ~ 29%. However, after cycling at 55 °Cthecarbonconcentration does not significantly change for the electrode cycled with the standard electrolyte while with added OMS the concentration of carbon increasesdramatically.After the initial formation cycling, the electrode extracted from the cell cycled with electrolyte containing OMS has a much higher concentration of fluorine (27%)than the electrode cycled with the standard electrolyte (5%). The electrodes extracted from cells containing the standard electrolyte have a steady increase of F as the cycling temperature is increased from 25 °C to 55 °C, consistent with $LiPF_6$ decomposition, as previously reported[53].On the contrary, the concentration of fluorine decreases upon increasing the cycling temperaturefor electrodes cycled with electrolyte containing OMS. This suggests that the decomposition of $LiPF_6$may be suppressed by the addition of OMS which is consistent with the superior capacity retention at elevated temperature (Figure 3.2). The oxygen concentration on theanodesafter formation cycling with the standard electrolyte is high (30%) and is decreased slightly after additional cycling at 25 °C and additional cycling at 55 °C (25%). The anode cycled with electrolyte containing OMS has much less O on the anode after the formation cycling (18%), consistent with OMS inhibition of EC reduction during formation cycling. Upon additional cycling at 25°C and 55°C, the electrodes extracted from cells containing electrolyte with added OMS have an increased concentration of oxygen, consistent with theincorporation of more lithium alkyl carbonates and lithium carbonate into SEI.The S concentrations for electrodes cycled with electrolyte containing OMS are low, ~ 1%, but constant, consistent with presence of lithium alkylsulfonatesin the SEI. In addition, the

concentration of Pgradually increases with increased cycling for anodes cycled with the standard electrolyte, while the concentration of P is relatively constant for anodes cycled with OMS, indicating that OMS inhibits $LiPF_6$ decomposition at elevated temperature. Interestingly, the Li concentration on the anode cycled with OMS is significantly lower than on the anode with standard electrolyte after cycling at 55°C, suggesting lower concentrations of lithium salts on the surface of the electrode.

Conclusion

The effect of the electrolyte additive 3-epoxypropyl methanesulfonate(OMS) has been investigated in graphite/NMC cells. Incorporation of OMS results in improved capacity retention and coulombic efficiency upon cycling at elevated temperature (55 °C). Incorporation of OMS also results in a slight decrease in cell impedance. Electrochemical analysis suggests that OMS reacts on the anode surface. Ex-situ surface analysis of cells cycled with and without OMS has been conducted to provide insight into the effect of OMS on the structure of the anode SEI. Incorporation of OMS inhibits the generation of lithium alkyl carbonates and results in the generation of lithium alkyl sulfonates in the initial SEI after formation cycling. In addition, the presence of OMS improves the stability of the SEI for cells cycled at elevated temperature by inhibiting the decomposition of the lithium alkyl carbonates. The improved electrochemical performance and ex-situ surface analysis suggests that OMS may be a viable replacement for 1,3-propane sultone (PS) in lithium-ion battery electrolytes.

Reference

1. K. Xu, *Chemical Reviews* (2014).
2. Y. P. Wu, E. Rahm and R. Holze, *J. Power Sources*, **114**, 228 (2003).
3. N. Dimov, S. Kugino and M. Yoshio, *J. Power Sources*, **136**, 108 (2004).
4. V. Aravindan, Y. S. Lee and S. Madhavi, *Adv Energy Mater*, **5**, 1402225 (2015).
5. S. Menne, M. Schroeder, T. Vogl and A. Balducci, *J. Power Sources*, **266**, 208 (2014).
6. L. Qie, W. M. Chen, Z. H. Wang, Q. G. Shao, X. Li, L. X. Yuan, X. L. Hu, W. X. Zhang and Y. H. Huang, *Advanced Materials*, **24**, 2047 (2012).
7. P. He, H. Yu, D. Li and H. Zhou, *J. Mater. Chem.*, **22**, 3680 (2012).
8. J. Xiao, N. A. Chernova and M. S. Whittingham, *Chem. Mater.*, **20**, 7454 (2008).
9. W. Liu, P. Oh, X. Liu, M. J. Lee, W. Cho, S. Chae, Y. Kim and J. Cho, *Angewandte Chemie International Edition*, **54**, 4440 (2015).
10. J. Y. Song, Y. Y. Wang and C. C. Wan, *J. Power Sources*, **77**, 183 (1999).
11. W. Li and J. R. Dahn, *J. Electrochem. Soc.*, **142**, 1742 (1995).
12. L. Yang, B. Ravdel and B. L. Lucht, *Electrochem Solid St*, **13**, A95 (2010).
13. M. Armand, F. Endres, D. R. MacFarlane, H. Ohno and B. Scrosati, *Nat. Mater.*, **8**, 621 (2009).
14. L. Suo, Y. S. Hu, H. Li, M. Armand and L. Chen, *Nature Communications*, **4**, 1481 (2013).
15. K. Xu, B. Deveney, K. Nechev, Y. Lam and T. R. Jow, *J. Electrochem. Soc.*, **155**, A959 (2008).

16. M. Q. Xu, L. Zhou, D. Chalasani, S. Dalavi and B. L. Lucht, *J. Electrochem. Soc.*, **158**, A1202 (2011).

17. S. Shui Zhang, *Electrochem. Commun.*, **8**, 1423 (2006).

18. S. Zhou, H. Han, J. Nie, M. Armand, Z. Zhou and X. Huang, *J. Electrochem. Soc.*, **159**, A1158 (2012).

19. S. Tsujioka, B. G. Nolan, H. Takase, B. P. Fauber and S. H. Strauss, *J. Electrochem. Soc.*, **151**, A1418 (2004).

20. N. N. Sinha, J. C. Burns and J. R. Dahn, *J. Electrochem. Soc.*, **160**, A709 (2013).

21. J. C. Burns, N. N. Sinha, G. Jain, H. Ye, C. M. VanElzen, E. Scott, A. Xiao, W. M. Lamanna and J. R. Dahn, *J. Electrochem. Soc.*, **161**, A247 (2014).

22. K. Abe, K. Miyoshi, T. Hattori, Y. Ushigoe and H. Yoshitake, *J. Power Sources*, **184**, 449 (2008).

23. S. S. Zhang, *J. Power Sources*, **163**, 567 (2006).

24. M. Sano, T. Hattori, T. Hibino and M. Fujita, *Electrochem. Solid-State Lett.*, **10**, A270 (2007).

25. L. El Ouatani, R. Dedryvère, C. Siret, P. Biensan, S. Reynaud, P. Iratçabal and D. Gonbeau, *J. Electrochem. Soc.*, **156**, A103 (2009).

26. G. Venugopal, J. Moore, J. Howard and S. Pendalwar, *J. Power Sources*, **77**, 34 (1999).

27. X. Huang, *J. Solid State Electrochem.*, **15**, 649 (2011).

28. J. A. Choi, S. H. Kim and D. W. Kim, *J. Power Sources*, **195**, 6192 (2010).

29. T. H. Cho, T. Sakai, S. Tanase, K. Kimura, Y. Kondo, T. Tarao and M. Tanaka, *Electrochem. Solid-State Lett.*, **10**, A159 (2007).

30. J. Vetter, P. Novák, M. R. Wagner, C. Veit, K. C. Möller, J. O. Besenhard, M. Winter, M. Wohlfahrt-Mehrens, C. Vogler and A. Hammouche, *J. Power Sources*, **147**, 269 (2005).
31. J. Shim, R. Kostecki, T. Richardson, X. Song and K. A. Striebel, *J. Power Sources*, **112**, 222 (2002).
32. S. S. Zhang, K. Xu and T. R. Jow, *J. Power Sources*, **115**, 137 (2003).
33. Q. Wang, P. Ping, X. Zhao, G. Chu, J. Sun and C. Chen, *J. Power Sources*, **208**, 210 (2012).
34. E. Peled, *J. Electrochem. Soc.*, **126**, 2047 (1979).
35. Y. Matsumura, S. Wang and J. Mondori, *J. Electrochem. Soc.*, **142**, 2914 (1995).
36. C. L. Campion, W. Li and B. L. Lucht, *J. Electrochem. Soc.*, **152**, A2327 (2005).
37. M. Xu, L. Zhou, L. Hao, L. Xing, W. Li and B. L. Lucht, *J. Power Sources*, **196**, 6794 (2011).
38. J. Xia, N. N. Sinha, L. P. Chen and J. R. Dahn, *J. Electrochem. Soc.*, **161**, A264 (2014).
39. J. C. Burns, R. Petibon, K. J. Nelson, N. N. Sinha, A. Kassam, B. M. Way and J. R. Dahn, *J. Electrochem. Soc.*, **160**, A1668 (2013).
40. L. Chen, K. Wang, X. Xie and J. Xie, *J. Power Sources*, **174**, 538 (2007).
41. X. Zhang, R. Kostecki, T. J. Richardson, J. K. Pugh and P. N. Ross, *J. Electrochem. Soc.*, **148**, A1341 (2001).
42. G. H. Wrodnigg, J. O. Besenhard and M. Winter, *J. Electrochem. Soc.*, **146**, 470 (1999).

43. R. Chen, F. Wu, L. Li, Y. Guan, X. Qiu, S. Chen, Y. Li and S. Wu, *J. Power Sources*, **172**, 395 (2007).

44. G. H. Wrodnigg, T. M. Wrodnigg, J. O. Besenhard and M. Winter, *Electrochem. Commun.*, **1**, 148 (1999).

45. W. Yao, Z. Zhang, J. Gao, J. Li, J. Xu, Z. Wang and Y. Yang, *Energ Environ Sci*, **2**, 1102 (2009).

46. Sano and S. Maruyama, *J. Power Sources*, **192**, 714 (2009).

47. Li, M. Xu, T. Li, W. Li and S. Hu, *Electrochem. Commun.*, **17**, 92 (2012).

48. M. Q. Xu, W. S. Li and B. L. Lucht, *J. Power Sources*, **193**, 804 (2009).

49. B. Ulland, M. Finkelstein, E. K. Eisburger, J. M. Rice and J. H. Weisburger, *Nature*, **230**, 460 (1971).

50. B. Zhang, M. Metzger, S. Solchenbach, M. Payne, S. Meini, H. A. Gasteiger, A. Garsuch and B. L. Lucht, *The Journal of Physical Chemistry C* (2015).

51. M. Xu, L. Zhou, Y. Dong, Y. Chen, J. Demeaux, A. D. MacIntosh, A. Garsuch and B. L. Lucht, *Energ Environ Sci*, **9**, 1308 (2016).

52. Y. Dong, J. Demeaux, Y. Zhang, M. Xu, L. Zhou, A. D. MacIntosh and B. L. Lucht, *J. Electrochem. Soc.*, **164**, A128 (2017).

53. M. Y. Nie, D. Chalasani, D. P. Abraham, Y. J. Chen, A. Bose and B. L. Lucht, *J. Phys. Chem. C*, **117**, 1257 (2013).

54. L. Bodenes, R. Dedryvere, H. Martinez, F. Fischer, C. Tessier and J. P. Peres, *J. Electrochem. Soc.*, **159**, A1739 (2012).

55. M. Andersson and K. Edstrom, *J. Electrochem. Soc.*, **148**, A1100 (2001).

56. K. Edstrom, M. Herstedt and D. P. Abraham, *J. Power Sources*, **153**, 380 (2006).

57. D. Aurbach, B. Markovsky, A. Shechter, Y. EinEli and H. Cohen, *J. Electrochem. Soc.*, **143**, 3809 (1996).

Table 3.1 Element concentrations by XPS

	C		F		O		S		P		Li	
	Standard	2% OMS	Standard	2% OMS	Standard	2% OMS	Standard	2% OMS	Standard	2% OMS	Standard	2% OMS
Formation	21%	22%	5%	27%	30%	18%	-	1%	1%	2%	43%	30%
Post-cycle 25 °C	30%	21%	10%	12%	25%	27%	-	2%	1%	2%	35%	35%
Post-cycle 55 °C	24%	41%	11%	9%	25%	29%	-	1%	4%	3%	36%	17%

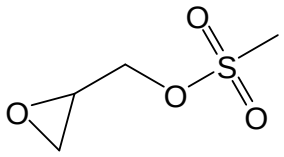

OMS

2, 3-epoxypropyl methanesulfonate

Figure 3.1 Molecular formula of OMS

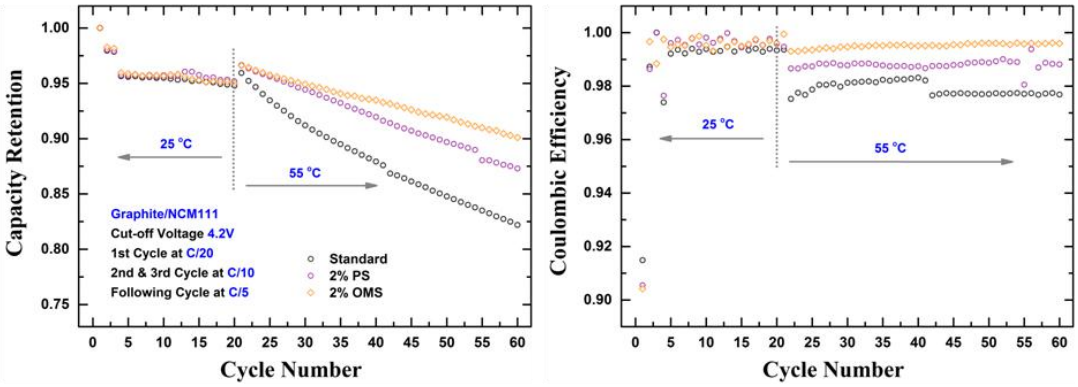

Figure 3.2 Galvanostatic cycling performance of the electrolytes with OMS

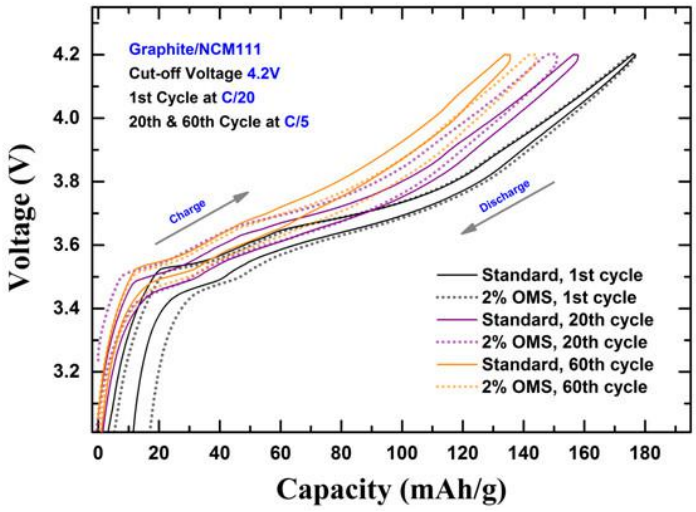

Figure 3.3 Charge/discharge voltage profiles of graphite/NCM with standard and 2 wt. % OMS electrolyte

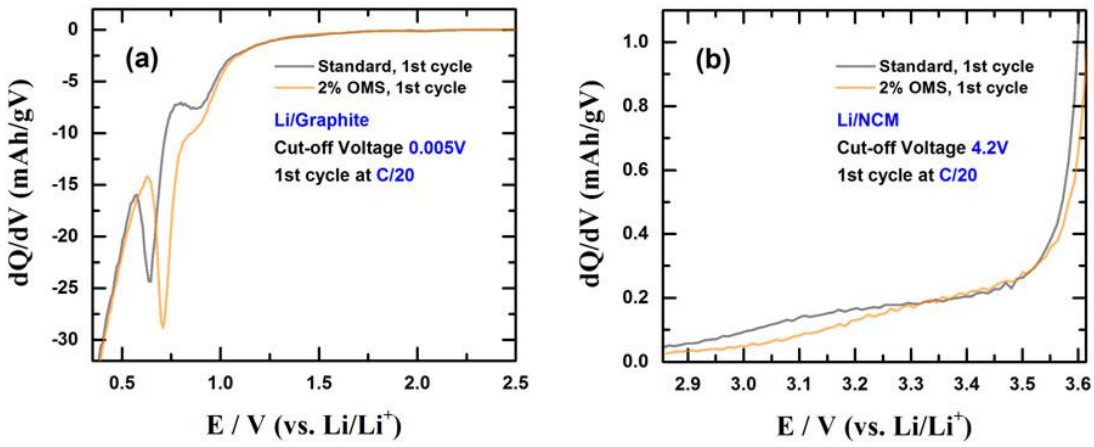

Figure 3.4 Differential capacity plots of Li/graphite (a) and Li/NCM (b)

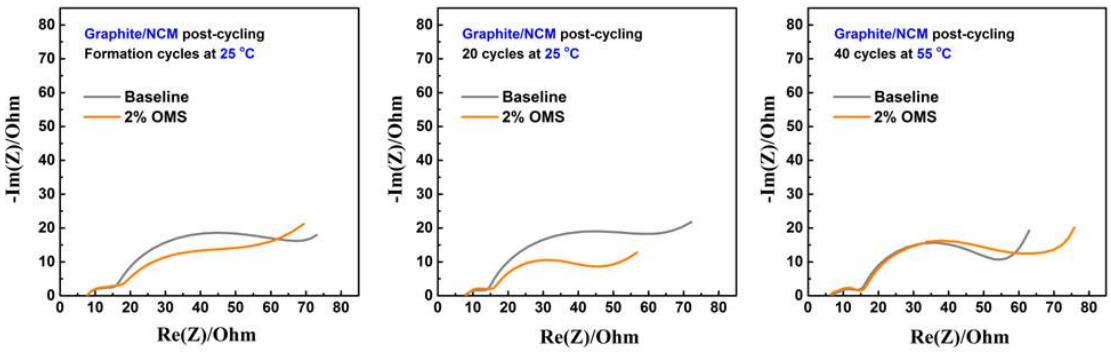

Figure 3.5 PEIS measurement of the cells cycled with OMS

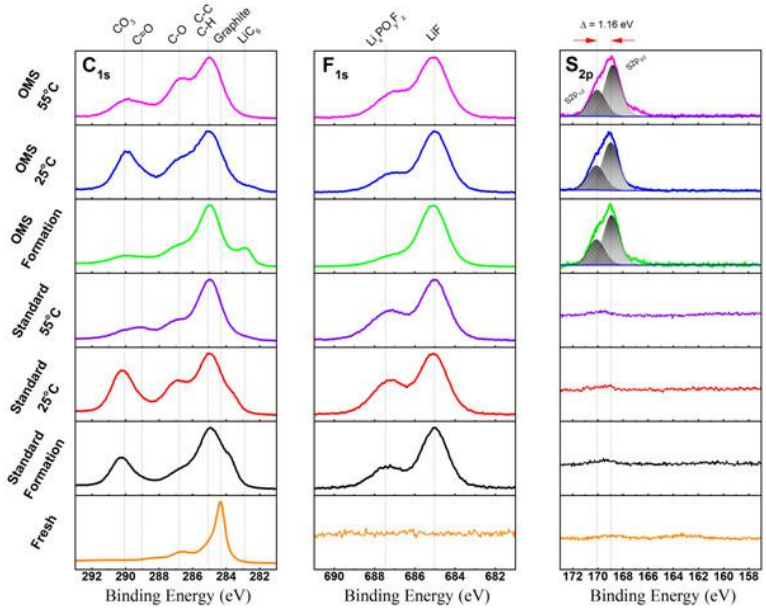

Figure 3.6 XPS analysis on the anodes cycled with OMS

CHAPTER4

Understanding Electrolyte Degradation of High Nickel NCM/Graphite Cells

Bo Zhang[a], Brett L. Lucht[a,*]

[a]*Department of Chemistry, University of Rhode Island, Kingston, RI 02881, USA*

The following chapter is in preparation for submission and presented here in manuscript format

Abstract

High nickel lithium-nickel-cobalt-manganese (NCM) metal oxide cathode material (such as, $LiNi_{0.8}Co_{0.1}Mn_{0.1}O_2$) has demonstrated prominent energy density over the years, while the gas evolution accompanied with elevated temperature and/or high voltage cycling is not fully understood yet. In this work, a comparison study of elevated temperature cycling was conducted on NCM111, NCM523, NCM622 and NCM811. Electrochemical impedance spectroscopy (EIS) was used to determine post-cycle cell impedance with various cathode materials. Surface analysis techniques (XPS and FTIR) were performed on the electrodes harvested from cycled coin cells. We further proposed a simple additive screening method using GC-MS to investigate electrolyte transesterification products and monitor gas evolution while incorporating novel electrolyte additives.

Introduction

The growing concern in global warming and the increasing demand of energy storage in consumer electronics and electric vehicles (EV) require high energy density Lithium-ion batteries (LIBs) and thus the according active materials [1, 2]. Lithium-nickel-cobalt-manganese oxide (NCM) cathode materials are considered as one of the most promising candidates in energy storage for this purpose [3, 4] and especially nickel-rich NCM, such as $LiNi_{0.5}Co_{0.2}Mn_{0.3}O_2$ (NCM523) [5-8], $LiNi_{0.6}Co_{0.2}Mn_{0.2}O_2$ (NCM622) [9-13], $LiNi_{0.65}Co_{0.25}Mn_{0.1}O_2$ [14], $LiNi_{0.65}Co_{0.08}Mn_{0.27}O_2$ [15] or $LiNi_{0.8}Co_{0.1}Mn_{0.1}O_2$ (NCM811) [16-18] are employed as a prominent cathode materials in recent years, due to their large energy density and lower cost compared to

$LiNi_{0.33}Co_{0.33}Mn_{0.33}O_2$ (NCM111) [19-21]. Nevertheless, the superiority in energy density of the higher nickel content is accompanied with several drawbacks, such as structural instability and gas evolution accompanied with enhanced electrolyte degradation and increasing internal cell pressure [1, 21-25]. A known degradation mechanism of the electrolyte solvents is the transesterification [26-29]. Here, ethyl methyl carbonate (EMC) undergoes a transesterification reaction into dimethyl carbonate (DMC) and diethyl carbonate (DEC) [30].

A simple and efficient method to reduce electrolyte degradation is the use of additives in carbonate based electrolytes combating the capacity retention loss, efficiency deterioration and operational safety compromise in LIB systems [31-34].

Within this work NCM materials with different nickel contents are investigated regarding their electrochemical stability. In addition, the surface of cathode and anode electrodes is investigated by FTIR and XPS to determine the effect of increasing nickel content on the nature of the surface film after cycling and thus the correlation to the electrochemical data. However, those differences are not always significant, thus other techniques needed to be found to understand the electrochemical differences of different nickel contents. In order to investigate the transesterification mechanism described earlier, gas chromatography mass spectrometry (GC-MS) of the cycled electrolyte of NCM samples with the biggest difference in cycling stability was measured. Using this technique not only the transesterification products can be investigated qualitatively and quantitatively, but also the consumption of additives can be monitored. Two additives, namely succinonitrile (SN) and 1,3-propane sultone (PS) have been studied by GC-MS in addition to the electrochemical analysis.

Experimental

CellAssembly

Graphite, $LiNi_{0.8}Co_{0.1}Mn_{0.1}O_2$ (NCM811) and $Li(Ni_{0.33}Co_{0.33}Mn_{0.33})O_2$ (NCM111)electrodes were prepared by ELEXEL. The positive electrode NCM111 and NCM811 are composed of 93 wt% active material, 3 wt% conductive carbon Super C65, and 4 wt% poly(vinylidenedifluoride) (PVDF) binder. The negative electrode is composed of 95.7 wt% graphite with 0.5 wt% carbon Super C65 and 3.8 wt% binder composed of carboxymethyl cellulose (CMC) and styrene butadiene rubber (SBR). All electrodes are calendered. Positive and negative electrode sheets were cut into a diameter of 13.7 mm and 15 mm, respectively. The NCM111 cathode loading is 12.3 mg/cm^2. The NCM811 cathode loading is 10.1mg/cm^2. The anode loading is 12.1 mg/cm^2. The graphite anode / NCM111 cathode area capacity ratio is 1.13, whereas the graphite/NCM811 cathode area capacity ratio is 1.10. All electrodes were dried in a vacuum oven for 24 hours at 110 °C. A baseline electrolyte of 1.2M lithium hexafluorophosphate ($LiPF_6$) in EC/EMC (3:7, v/v) (BASF; water content below 50 ppm) was used.

Coin cells (CR2032) were assembled with a stack of three separators (polyolefin, glass fiber and polyolefin) drenched with 105 µL of freshly prepared electrolyte in an Ar filled glove box (water content ≤0.01 ppm).

GalvanostaticCycling

The general cell cycling protocols are presented as follows (unless otherwise indicated in the context, respectively). The coin cells were thereafter cycled between 4.2 V and 3.0 V using an Arbin BT2000 battery cycler. First group of cells underwent

initial formation cycles including C/20 for the first cycle, C/10 for the second and third cycle, followed by 17 cycles with a rate of C/5 at 25°C. Sequentially, another 50 cycles were performed at 45°C with a rate of C/5.

Electrochemical Impedance Spectroscopy (EIS)

The general EIS protocols are presented as follows (unless otherwise indicated in the context, respectively). The potentiostatic electrochemical impedance measurements were performed using a BioLogic VSP at 25°C (± 1°C). The impedance of all coin cells was acquired at 3.0 V with a sinusoidal amplitude Va= 10mV and frequency range from 300kHzto 20mHz.

X-ray photoelectron spectroscopy (XPS)

After galvanostatic cycling cells were disassembled in an argon filled glove box. Electrodes (discharged state) were rinsed three times with anhydrous dimethyl carbonate (DMC) to remove residual electrolyte, prior to being thoroughly dried in a vacuum chamber at 25 °C. As discussed in our previous work, X-ray photoelectron spectroscopy (XPS) analysis was conducted on a Thermo K-Alpha system with a focused monochromatized Al Kα radiation (hυ = 1486.6 eV) beam under ultrahigh vacuum (8.1×10^{-8}Pa). The electrodes were transferred from the glove box to the XPS chamber via a customized vacuum sample holder. The spectra were collected with constant pass energy of 50 eV. XPS peaks were processed by ThermoAvantage v5.932. The hydrocarbon peak at 285 eV was selected as a binding energy reference for the peer peak assignment.

Attenuated Total Reflectance Fourier Transform Infrared Spectroscopy (ATR-FTIR)

Attenuated Total Reflectance Fourier Transform Infrared Spectroscopy (ATR-FTIR) was conducted on a Bruker Tensor 27 IR spectrometer with a germanium crystal (Pike MIRacle ATR accessory) with a room temperature DLaTGS detector. 256-scan with a spectral resolution of 4 cm^{-1}were acquired for each electrode under a constant nitrogen gas flow.

Gas Chromatography Mass Spectrometry (GC-MS)

After cycling cells were dissembled in argon filled glove box. All cell components (excluding lithium metal) were centrifuged (4000 rpm for 5 min) to collect the electrolyte. The electrolyte was then extracted with 5 mL Dichloromethane and then with 1 mL distilled water for 10 min, respectively. The quenching was required to remove the salt $LiPF_6$ and prevent the degradation of GC column. The final supernatant was then filtered using a syringe filter with a polytetrafluoroethylene (PTFE) membrane and 0.45 µm pores. The diluted electrolyte was measured with a GC-MS unit consisted of a Algilent (6890 Series GC System and 5973N Mass Selective Detector) equipped with a split/split-less injector, a 30-m column with an inner diameter of 0.25 mm, as well as a single-quadrupole mass spectrometer equipped with an electron impact ionization module. Helium was used as carrier gas at a constant flow rate of 23.7 mL min^{-1}. The injection temperature was set to 40 ºC, and the oven temperature was programmed with a ramp to 250 ºC at 20 ºC min^{-1}. The transfer line was set to 250 ºC, the ion source to 230 ºC, and the electron energy to 70 eV.

Results and Discussion

Electrochemical Measurement

Figure 4.1a shows the specific discharge capacity of NCM / Graphite cells with different nickel content. As expected, NCM811 shows a higher specific discharge capacity than NCM111, NCM523 and NCM622. However, this additional capacity is accompanied by a higher capacity fading. Both NCM111 and NCM523 have similar first cycle efficiency (Figure 4.1b) around 87%, nearly 6% higher than those of NCM622 and NCM811. Upon cycling NCM111 and NCM523 have the highest efficiency close to 99.8%, whereas NCM622 has the least efficiency around 98%, followed by NCM811 at 98.9%. Overall, as indicated in Figure 4.1c, all NCM / Graphite cells have almost paralleled capacity retention slopes, a similar capacity fading trend upon cycling. Several irregular data points are due to accidental power outages occurred during the cycling.

Additionally, we have acquired the cell impedance after 200 cycles of galvanostatic cycling at 45°C (Figure 4.2). The data indicate that nickel-rich NCM cathodes show unfavorable cell impedance growth, ensuing compromised cycling performance and stability at elevated temperature which is in good agreement with the slightly higher capacity fading of NCM 811 / Graphite cells.

Figure 4.3 shows the differential capacity curves of NCM / Graphite cells upon cycling at elevated temperature. Both NCM111 and NCM811 cells have a decrease in reversible capacity. While most peaks of NCM 811 and NCM111 are comparable, NCM811 has an additional well-defined peak at 4.13V mainly associated with the oxidation of Ni^{2+} [35, 36].

Further, electrochemical impedance measurements were conducted on NCM / Graphite cells during the first formation cycle. Prior to EIS, cells were charged up to different potential at 3.6 V, 3.8 V, 4.0 V, 4.1 V, 4.15 V and 4.2 V with a taper step at C/100 (Figure 4.4) corresponding to the oxidation/reduction reaction (see also Figure 4.3). A generic decreasing trend in cell impedance is observed as the voltage increases. The NCM111 / Graphite cell has clear trend of decreasing charge transfer resistance as the voltage reaches higher. The NCM811 / Graphite has a similar trend in cell impedance as the voltage increases up to 4.1 V. However, a reversing growth in cell impedance is observed after NCM811 / Graphite cell is charged above 4.15V.

Surface Analysis

XPS analysis was conducted on NCM cathodes during the 1st charge (Figure 4.5 and Figure 4.6). The graphite peak 284.3 eV in C1s spectrum was selected as the internal reference. Both fresh C1s spectra of NCM111 and NCM811 appear to be very similar. The fresh cathode is primarily dominated by PVDF binder. However, the O1s spectra indicates that fresh NCM811 has a larger region of C=O/C-O species, comparing to fresh NCM111. After being charged up to 4.15 V, the O1s spectrum suggests the evolution of organic species (C=O/C-O) on NCM111 surface as the CEI layer is formed. On the other hand, there is no significant difference observed on the NCM811 electrode after the 1st charge to 4.15 V.

As depicted in Figure 4.7, all anodes are very similar in terms of C1s, O1s, P2p, Ni2p, Co2p, Mn2p and Li1s spectra after 200 cycles at 45°C, which is in agreement with similar cell cycling performance under the same circumstance. However, certain variations are observed in F1s spectra as indicated in Figure 4.8. There is no particular

trend in behavior associated with varying the nickel content in the cathode. The detected difference in LiF contribution could result from the accidental decomposition process of the electrolyte residue. Small amounts of transition metals are deposited on the anodes. In addition, XPS spectra of the NCM cathodes after 200cycles at 45°C are shown in Figure 4.8. Although there is a small (well defined metal oxide peak at 529 eV in O1s spectra) amount of electrolyte decomposition (for instance, LiF at 685 eV in F1s spectra) on the surface, no significant difference can be observed among the cathodes with varying nickel contents.

Of the same electrodes IR spectra were taken after 200 cycles (Figure 4.9). There are no significant differences observed on the anode. All of the anodes have a significant concentration of Li_2CO_3 on the surface as evidenced by the absorption at ~1450 cm^{-1}. On the other hand, the IR of the cycled cathodes is illustrated in Figure 4.10. All fresh cathodes are occupied by similar peaks related to the PVDF binder. After 200cycles at 45°C, all cathodes still appear similar, despite of the variations in the peak intensity.

The surface analysis of NCM / Graphite cells using NCM with different nickel contents suggests that changes to the surface chemistry are not likely the source of the difference in electrochemical stability. Thus a more detailed analysis of the electrolyte and the electrolyte degradation products has been performed.

Electrolyte Extraction Analysis

GC-MS analysis has been performed on NCM111 / Graphite and NCM811 / Graphite cells in order to correlate the previous electrochemical data and surface analysis with the degradation products of the electrolyte.

In Figure 4.11, the spectra of the freshly prepared standard electrolyte (1.2 M $LiPF_6$ in EC/EMC 3/7) after extracting the salt with water is presented compared to pure EC and pure EMC (dichloromethane is present due to the sample preparation). All components are analyzed by GC-MS and structurally assigned through matching to the National Institutes of Standards (NIST) library. The peak at 1.957 min is ascribed to EMC, whereas the peak at 2.797 is attributed to EC.

As shown in Figure 4.12, the peak b and d are assigned to ethyl methyl carbonate (EMC) and ethylene carbonate (EC), respectively. The transesterification products of EMC and EC are dimethyl carbonate (DMC, peak a) and diethyl carbonate (DEC, peak c). The dimerization products of DMC with EC, EMC with EC and DEC with EC are ethylene glycol bis-(methyl carbonate) (DMOHC, peak e), ethylene glycol (ethyl methyl carbonate) (EMOHC, peak f), and ethylene glycol bis-(ethyl carbonate) (DEOHC, peak g). The GC-MS results are in good agreement with the observation by Petibon et. al. [5]. Based on the intensity of the peaks of transesterification and dimerization products mentioned-above, we can draw a conclusion that nickel-rich NCM811 / Graphite cells have more electrolyte decomposition than NCM111 / Graphite cells under a similar cycling circumstance (1st cycle with a rate of C/20, and following cycles with a rate of C/3 at 45°C) which might lead to a higher capacity fading and therefore a lower capacity retention.

Addressing the more intense electrolyte degradation the NCM / Graphite cells were cycled with an additive containing electrolyte, namely with 1,3-propane sultone (PS) and succinonitrile (SN). Figure 4.13 shows the cycling performance of those two

additives employed in the nickel-rich NCM811 / Graphite system, whereas Figure 4.14 shows the cycling data of the NCM111 / Graphite system.

In both scenarios of NCM811 and NCM111, the additive-free baseline and the additive-containing cells have comparable cycling performance in terms of discharge capacity and coulombic efficiency (Figure 4.13 and Figure 4.14). However, the cells cycled with SN outperform the rest of each group in terms of capacity retention by 5% for the NCM811 system and 4% for the NCM111 system (Figure 4.15), respectively.

As shown in Figure 4.16, the NCM811 cell cycled with 1% SN has a significant decrease in DMC and DEC (transesterification products) and a concomitant reduction in dimerization byproducts, indicating the incorporation of SN inhibits the electrolyte transesterification process by forming a good passivation layer on the electrodes. Similarly, the addition of PS also largely reduces the transesterification and dimerization reactions. Electrolyte extraction analysis by GC-MS on the NCM111employed system is demonstrated in Figure 4.17. A moderate decrease in transesterification is observed in the NCM111 / Graphite cells either cycled with PS or SN. It is noteworthy that the baseline of the NCM111 / Graphite cell had lower concentrations of transesterification and dimerization, comparing to an additive-free NCM811/graphite cell under a similar circumstance (Figure 4.12).

Conclusion

We have conducted an investigation of high nickel content NCM/Graphite coin cells in terms of cyclability, capacity retention, coulombic efficiency, and electrochemical behavior with or without electrolyte additive blends at elevated

temperature and surface analysis on those cycled electrodes via XPS and IR. At elevated temperature of 45 °C a general ~25% increase of specific capacity is delivered by NCM811/ Graphite cells, compared to NCM111 / Graphite cells due to the higher nickel content. However, the fading of NCM811 /Graphite cells is higher than that of NCM/111 cells which is in agreement with a more significant impedance growth. Since there were no significant differences observed by surface analysis techniques, the decomposition of the electrolyte to generate transesterification products most likely correlates to the electrochemical stability of NCM811. The presence of the transesterification products may also correlate with increases in gas evolution for cathodes with higher Ni content. The results of GC-MS analysis of the electrolyte after cycling confirm this theory that nickel-rich NCM811 has more intense transesterification and dimerization than NCM111 under a similar cycling condition. We have also determined that nickel-rich NCM811 cycled with succinonitrile (SN) has better cycling performance, as well as lower concentrations of transesterification / dimerization byproducts according to GC-MS analysis.

Reference

1. N. Nitta, F. Wu, J. T. Lee and G. Yushin, *Materials Today*, **18**, 252 (2015).
2. E. M. Erickson, C. Ghanty and D. Aurbach, *The Journal of Physical Chemistry Letters*, **5**, 3313 (2014).
3. Z. Liu, A. Yu and J. Y. Lee, *J. Power Sources*, **81–82**, 416 (1999).
4. Tsutomu and M. Yoshinari, *Chem. Lett.*, **30**, 642 (2001).
5. D. Wang, X. Li, Z. Wang, H. Guo, Z. Huang, L. Kong and J. Ru, *J. Alloys Compd.*, **647**, 612 (2015).
6. Y. Shi, M. Zhang, D. Qian and Y. S. Meng, *Electrochim. Acta*, **203**, 154 (2016).
7. S.-K. Jung, H. Gwon, J. Hong, K.-Y. Park, D.-H. Seo, H. Kim, J. Hyun, W. Yang and K. Kang, *Adv Energy Mater*, **4**, 1300787 (2014).
8. B. B. Berkes, A. Schiele, H. Sommer, T. Brezesinski and J. Janek, *J. Solid State Electrochem.*, **20**, 2961 (2016).
9. Y. Chen, Y. Zhang, B. Chen, Z. Wang and C. Lu, *J. Power Sources*, **256**, 20 (2014).
10. W. Cho, S.-M. Kim, J. H. Song, T. Yim, S.-G. Woo, K.-W. Lee, J.-S. Kim and Y.-J. Kim, *J. Power Sources*, **282**, 45 (2015).
11. N. Y. Kim, T. Yim, J. H. Song, J.-S. Yu and Z. Lee, *J. Power Sources*, **307**, 641 (2016).
12. F. Schipper, M. Dixit, D. Kovacheva, M. Talianker, O. Haik, J. Grinblat, E. M. Erickson, C. Ghanty, D. T. Major, B. Markovsky and D. Aurbach, *Journal of Materials Chemistry A*, **4**, 16073 (2016).
13. H. Kim, M. G. Kim, H. Y. Jeong, H. Nam and J. Cho, *Nano Lett.*, **15**, 2111 (2015).

14. Milewska, M. Molenda and J. Molenda, *Solid State Ionics*, **192**, 313 (2011).
15. E. M. Erickson, H. Bouzaglo, H. Sclar, K.-J. Park, B.-B. Lim, F. Schipper, C. Ghanty, J. Grinblat, B. Markovsky, Y.-K. Sun and D. Aurbach, *J. Electrochem. Soc.*, **163**, A1348 (2016).
16. J. Li, L. E. Downie, L. Ma, W. Qiu and J. R. Dahn, *J. Electrochem. Soc.*, **162**, A1401 (2015).
17. J. Yang and Y. Xia, *J. Electrochem. Soc.*, **163**, A2665 (2016).
18. J. Eom, M. G. Kim and J. Cho, *J. Electrochem. Soc.*, **155**, A239 (2008).
19. W. Liu, P. Oh, X. Liu, M. J. Lee, W. Cho, S. Chae, Y. Kim and J. Cho, *Angewandte Chemie International Edition*, **54**, 4440 (2015).
20. C. Julien, A. Mauger, K. Zaghib and H. Groult, *Inorganics*, **2**, 132 (2014).
21. Manthiram, B. Song and W. Li, *Energy Storage Materials*, **6**, 125 (2017).
22. Y. Ding, D. Mu, B. Wu, R. Wang, Z. Zhao and F. Wu, *Applied Energy*, **195**, 586 (2017).
23. S. M. Bak, E. Hu, Y. Zhou, X. Yu, S. D. Senanayake, S. J. Cho, K.-B. Kim, K. Y. Chung, X. Q. Yang and K. W. Nam, *Acs Appl Mater Inter*, **6**, 22594 (2014).
24. Y. Wang, J. Jiang and J. R. Dahn, *Electrochem. Commun.*, **9**, 2534 (2007).
25. H. U. Escobar-Hernandez, R. M. Gustafson, M. I. Papadaki, S. Sachdeva and M. S. Mannan, *J. Electrochem. Soc.*, **163**, A2691 (2016).
26. H. Yoshida, T. Fukunaga, T. Hazama, M. Terasaki, M. Mizutani and M. Yamachi, *J. Power Sources*, **68**, 311 (1997).
27. D. Aurbach, B. Markovsky, A. Rodkin, M. Cojocaru, E. Levi and H.-J. Kim, *Electrochim. Acta*, **47**, 1899 (2002).

28. S. E. Sloop, J. B. Kerr and K. Kinoshita, *J. Power Sources*, **119–121**, 330 (2003).

29. J.-Y. Eom, I.-H. Jung and J.-H. Lee, *J. Power Sources*, **196**, 9810 (2011).

30. R. Petibon, L. Rotermund, K. J. Nelson, A. S. Gozdz, J. Xia and J. R. Dahn, *J. Electrochem. Soc.*, **161**, A1167 (2014).

31. M. Xu, L. Zhou, Y. Dong, Y. Chen, J. Demeaux, A. D. MacIntosh, A. Garsuch and B. L. Lucht, *Energ Environ Sci*, **9**, 1308 (2016).

32. B. Zhang, M. Metzger, S. Solchenbach, M. Payne, S. Meini, H. A. Gasteiger, A. Garsuch and B. L. Lucht, *J. Phys. Chem. C*, **119**, 11337 (2015).

33. R. Petibon, L. Madec, L. M. Rotermund and J. R. Dahn, *J. Power Sources*, **313**, 152 (2016).

34. M. Börner, F. Horsthemke, F. Kollmer, S. Haseloff, A. Friesen, P. Niehoff, S. Nowak, M. Winter and F. M. Schappacher, *J. Power Sources*, **335**, 45 (2016).

35. C. Ghanty, B. Markovsky, E. M. Erickson, M. Talianker, O. Haik, Y. Tal-Yossef, A. Mor, D. Aurbach, J. Lampert, A. Volkov, J. Y. Shin, A. Garsuch, F. F. Chesneau and C. Erk, *ChemElectroChem*, **2**, 1479 (2015).

36. N. A. Chernova, M. Ma, J. Xiao, M. S. Whittingham, J. Breger and C. P. Grey, *Chem. Mater.*, **19**, 4682 (2007).

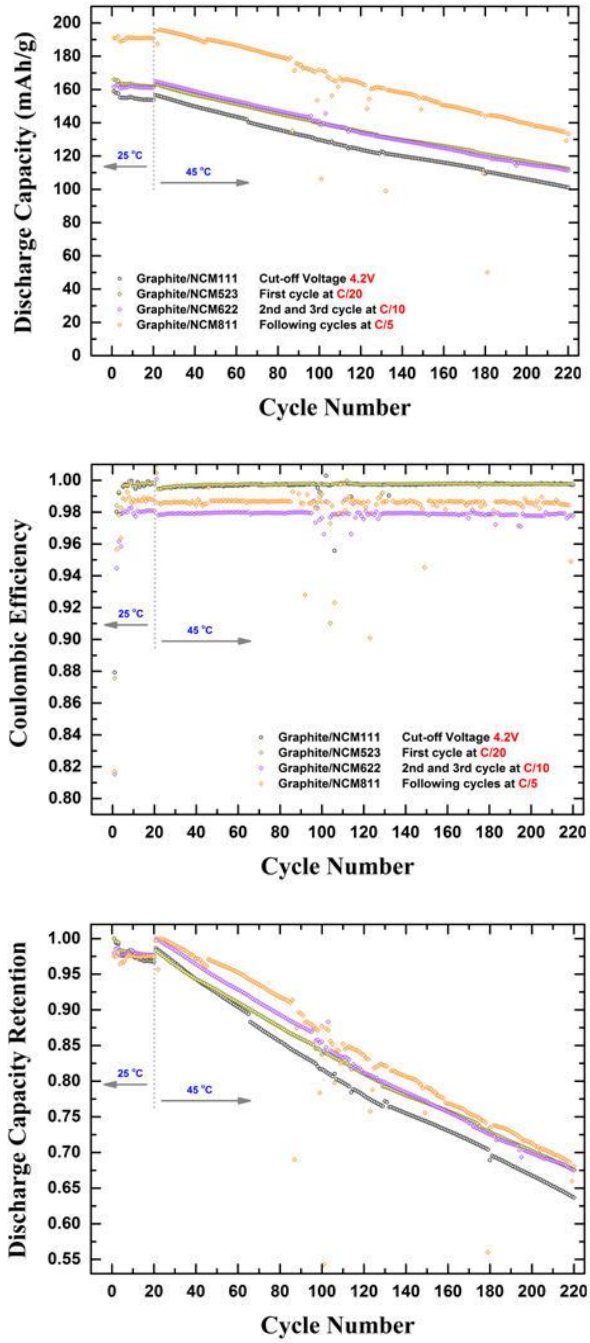

Figure 4.1 Galvanostatic cycling performance of graphite/NCM cells

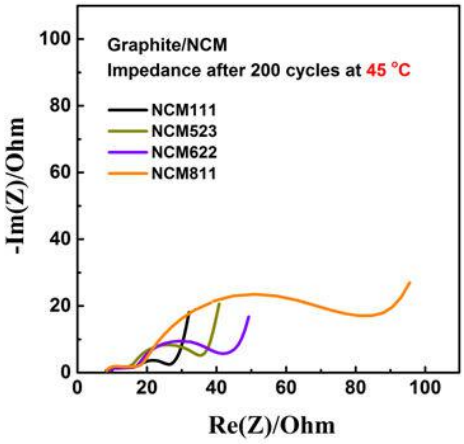

Figure 4.2 Post-cycle impedance measurements of graphite/NCM cells

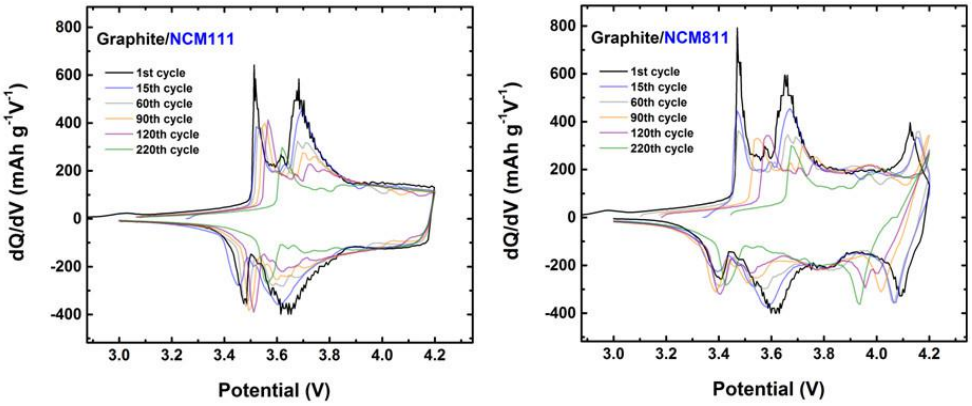

Figure 4.3 Differential capacity curves of graphite/NCM cells of selected cycles.

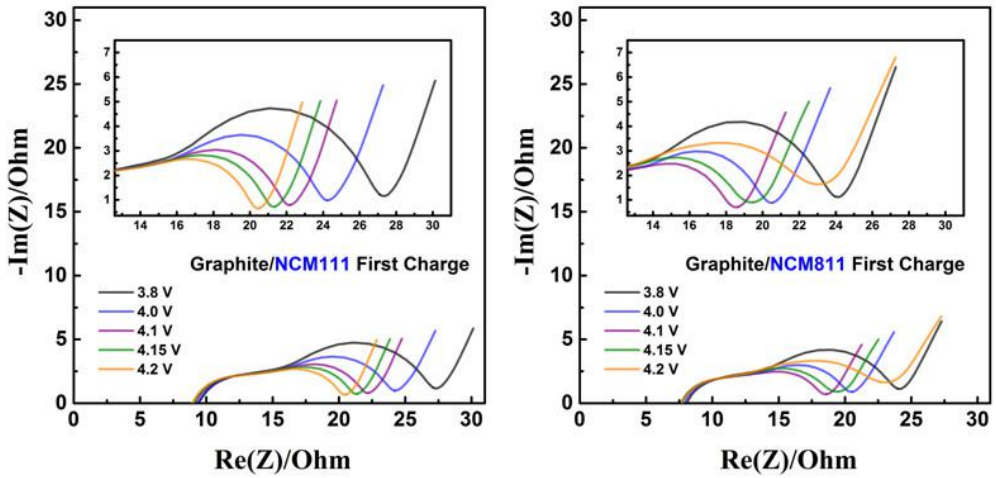

Figure 4.4 PEIS measurement of graphite/NCM cells during the first charge

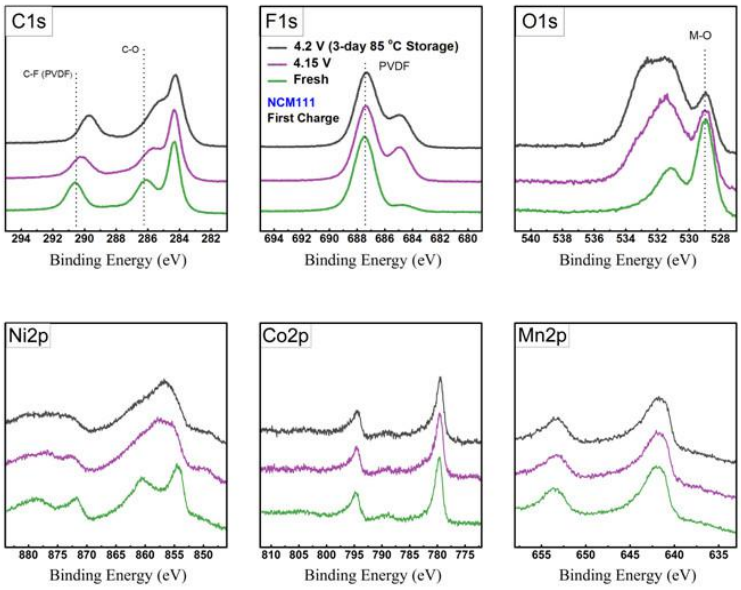

Figure 4.5 XPS analysis on NCM111 cathode after the 1st charge

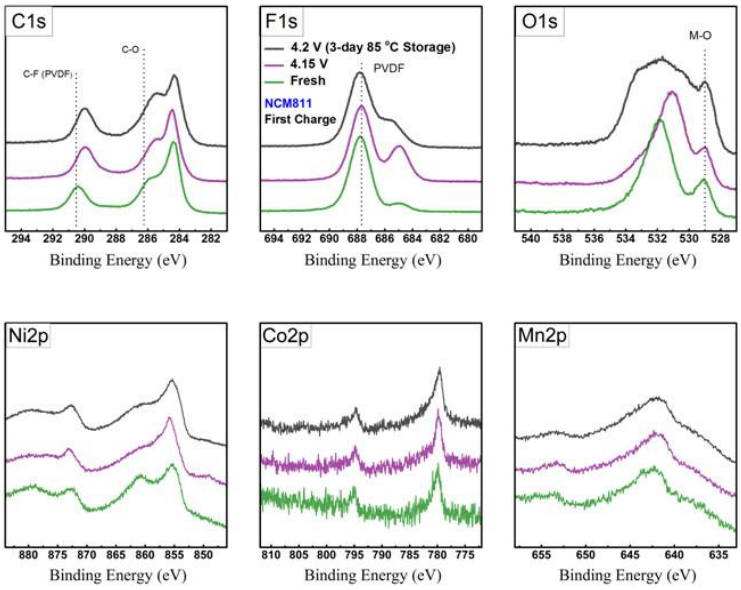

Figure 4.6 XPS analysis on NCM811 cathode after the 1st charge

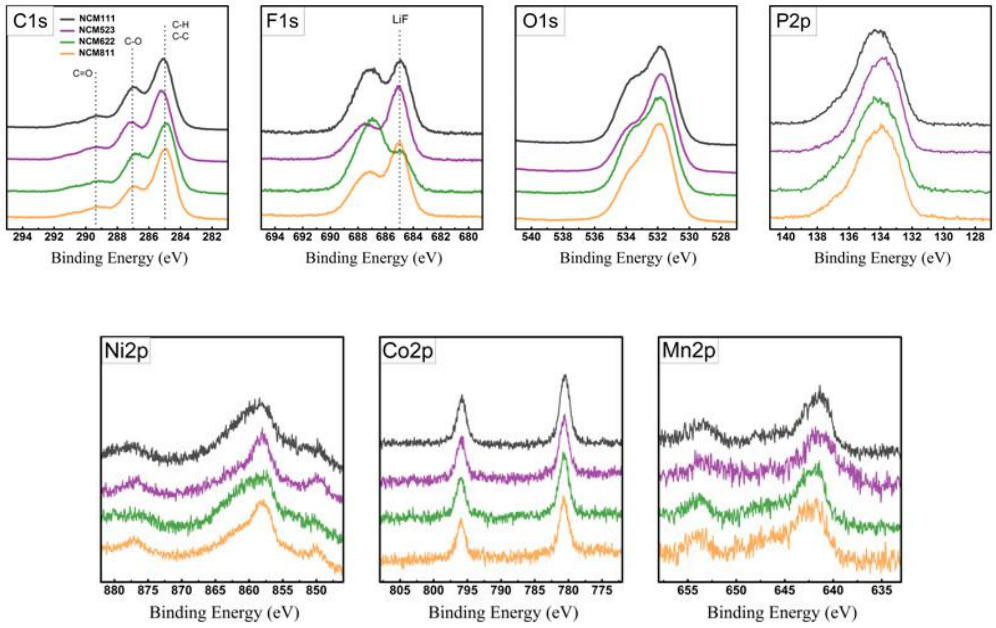

Figure 4.7 XPS analysis on the anodes after 200 cycles at 45°C

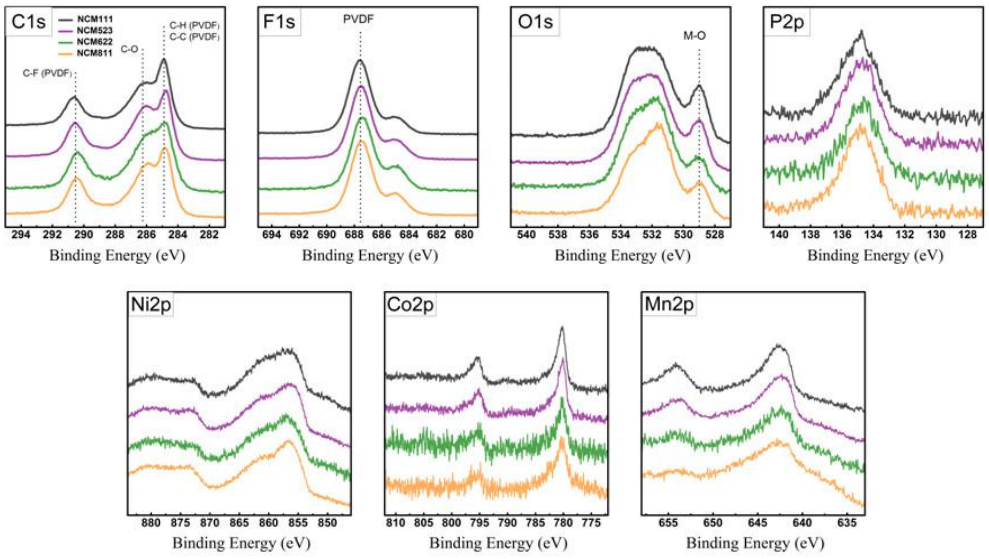

Figure 4.8 XPS analysis on NCM cathodes after 200 cycles at 45°C

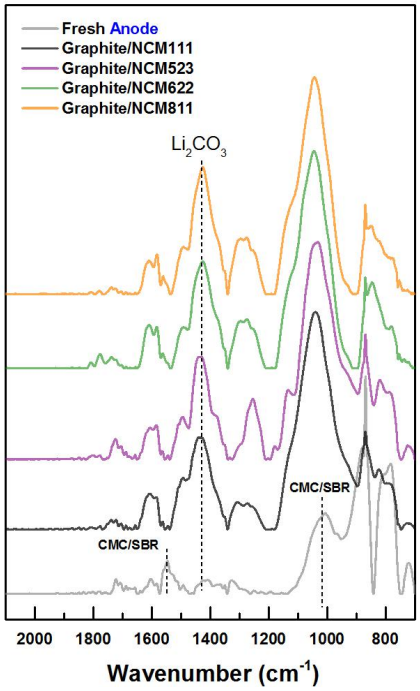

Figure 4.9 IR analysis on the anodes after 200 cycles at 45°C

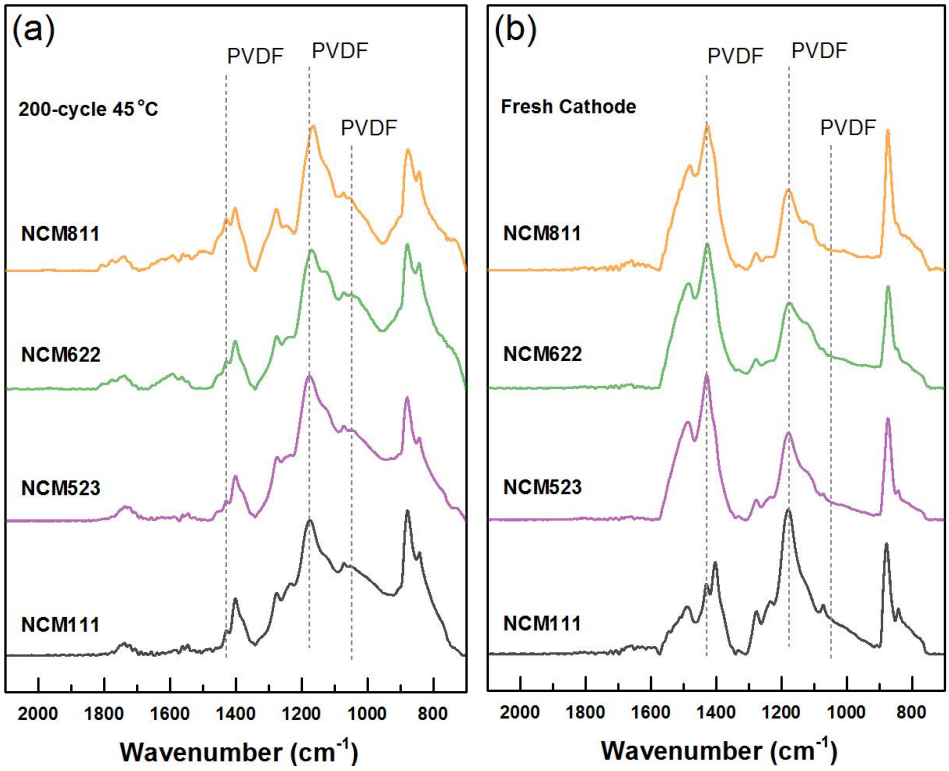

Figure 4.10 IR analysis on the NCM cathodes (a) after 200-cycle at 45°C and (b) fresh cathodes.

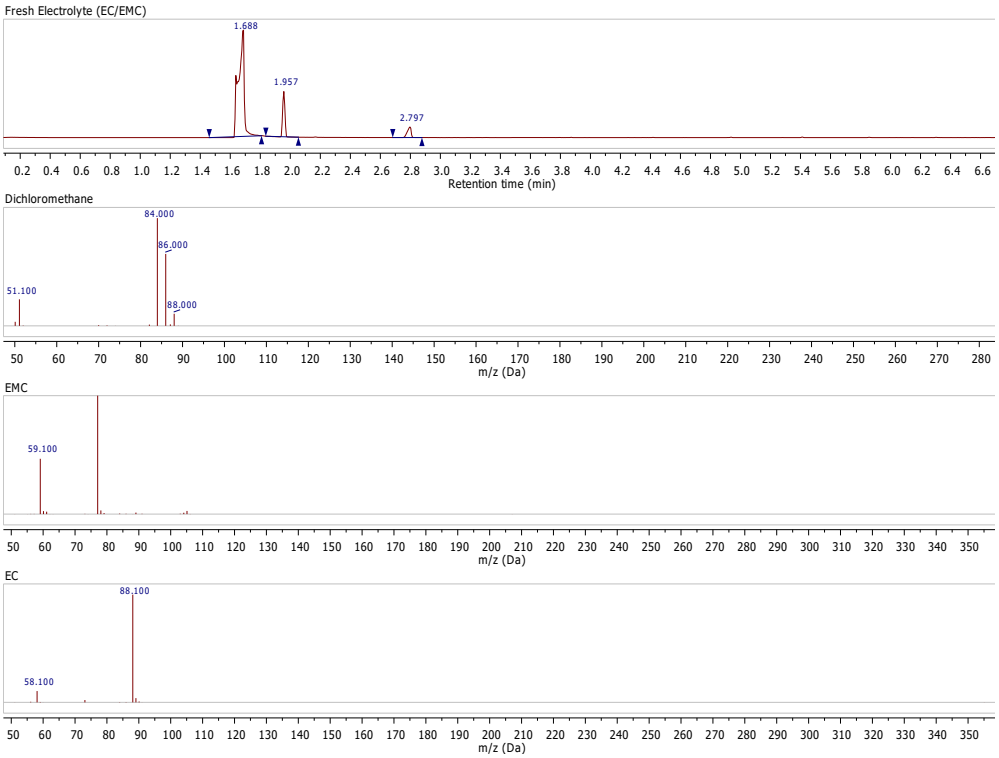

Figure 4.11 GC-MS of fresh electrolyte (1.2 M $LiPF_6$ in EC/EMC 3/7, v./v.) after quenching compared to dichloromethane, EC and EMC.

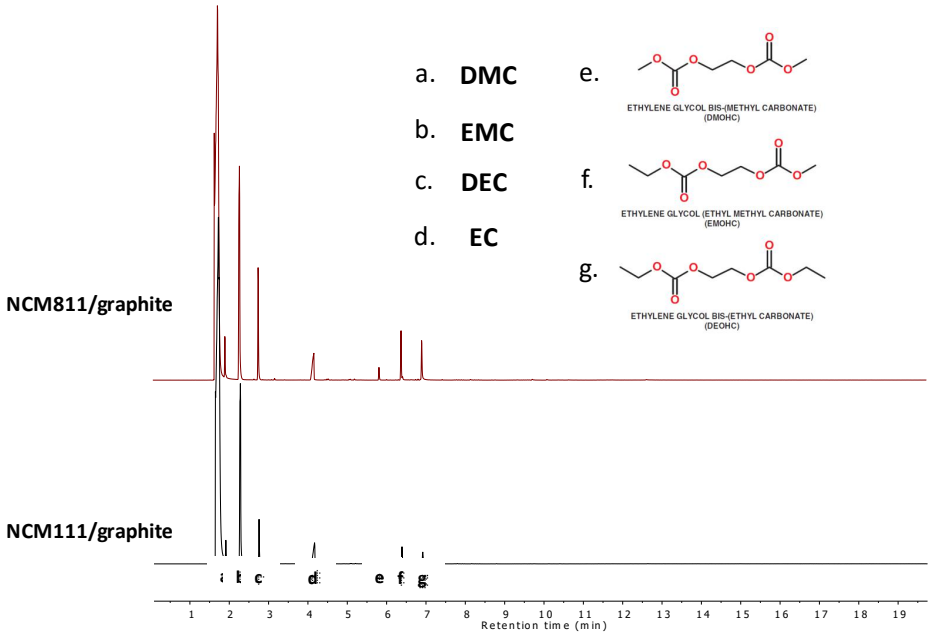

Figure 4.12 GC-MS analysis on the electrolytes extracted from graphite/NCM cells

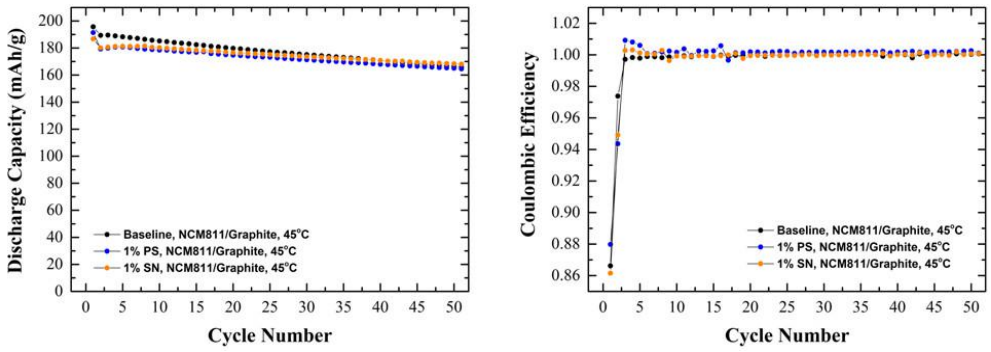

Figure 4.13 Galvanostatic cycling of graphite/NCM811 cells with PS or SN

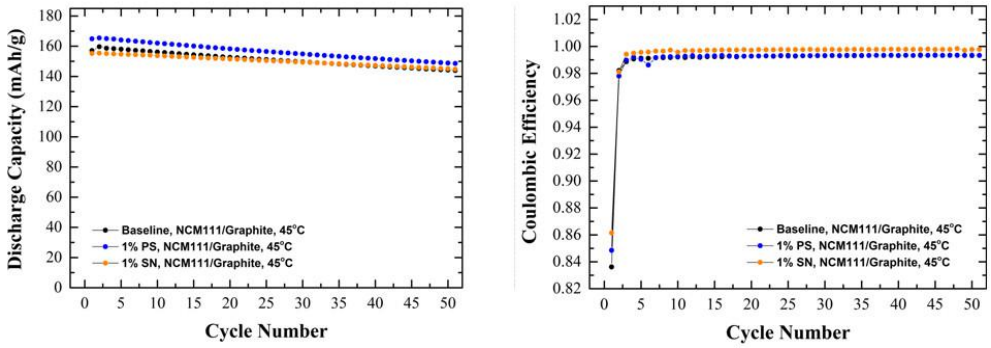

Figure 4.14 Galvanostatic cycling of graphite/NCM111 cells with PS or SN

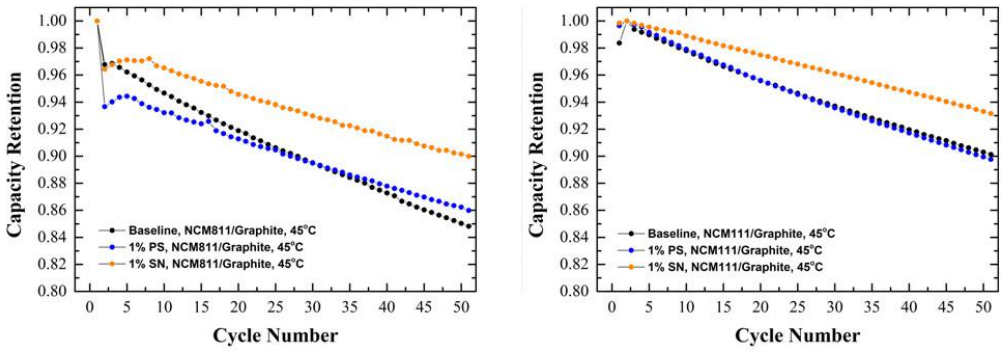

Figure 4.15 Capacity retention of graphite/NCMcells with PS or SN

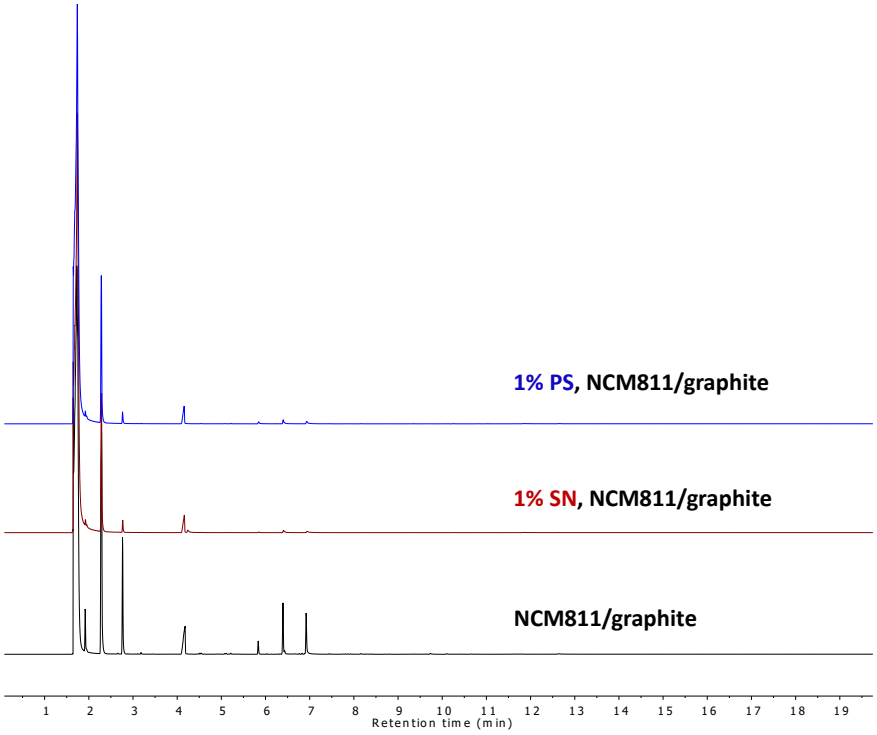

Figure 4.16 GC-MS on the electrolytes extracted from graphite/NCM811 cells cycled with PS or SN

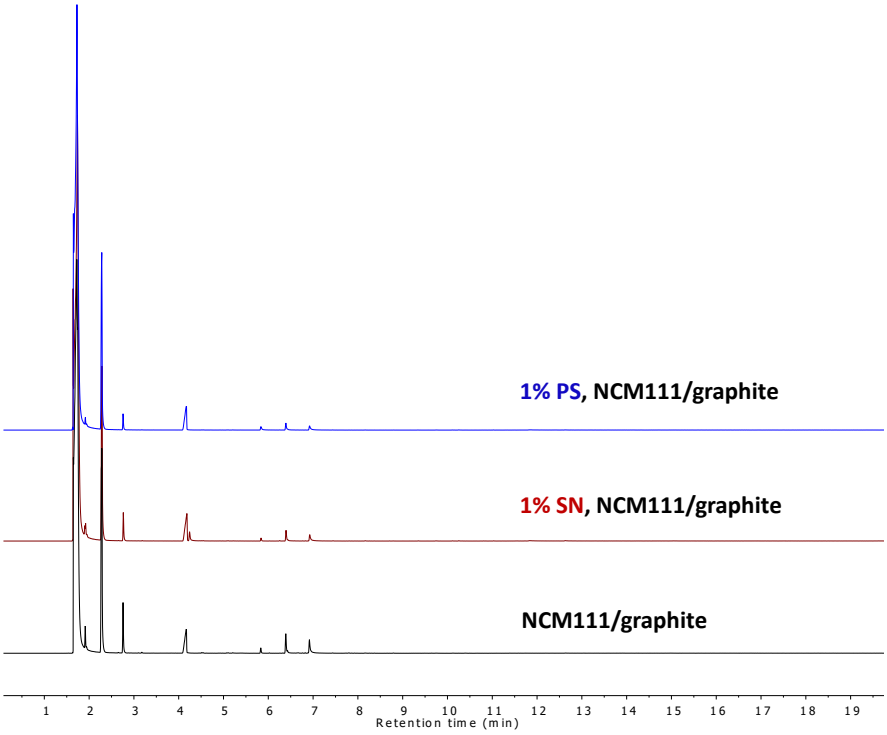

Figure 4.17 GC-MS on the electrolytes extracted from graphite/NCM111 cells cycled with PS or SN